Measurement of Retinal Vascular Permeability in a Rat Model Using Spectroscopic Optical Coherence Tomography

by

Woo Jhon Choi

B.S., Electrical and Computer Engineering
B.S., Biomedical Engineering
A.B., Physics
Duke University, 2009

MASSACHUSETTS INSTITUTE OF TECHNOLOGY
SEP 27 2011
LIBRARIES
ARCHIVES

Submitted to the
DEPARTMENT OF ELECTRICAL ENGINEERING AND COMPUTER SCIENCE
in partial fulfillment of the requirements for the degree of
MASTER OF SCIENCE in ELECTRICAL ENGINEERING AND COMPUTER SCIENCE

at the

MASSACHUSETTS INSTITUTE OF TECHNOLOGY

September 2011

© 2011 Massachusetts Institute of Technology. All rights reserved

Signature of Author: _____
Department of Electrical Engineering and Computer Science
September 2, 2011

Certified by: _____
James G. Fujimoto
Professor of Electrical Engineering and Computer Science
Thesis Supervisor

Accepted by: _____
Leslie A. Kolodziejski
Chair, Department Committee on Graduate Students

Measurement of Retinal Vascular Permeability in a Rat Model Using Spectroscopic Optical Coherence Tomography

by

Woo Jhon Choi

Submitted to the Department of Electrical Engineering and Computer Science on September 2, 2011 in partial fulfillment of the requirements for the degree of Master of Science in Electrical Engineering and Computer Science

Abstract

Optical coherence tomography (OCT), a diagnostic tool which can perform non-contact, non-invasive, cross-sectional imaging of the retina and anterior eye in real time, has dramatically improved in its resolution and speed in the recent years. In addition to the advancement in hardware, different OCT methods for functional measurements, such as Doppler OCT for quantifying blood flow and generating angiography using OCT phase information, polarization sensitive OCT for measuring intrinsic mechanical / optical tissue property using light of different polarizations, and spectroscopic OCT for measuring blood oxygenation using multiple wavelengths, have been demonstrated and developed.

In this thesis, a dual-wavelength spectroscopic OCT technique is investigated to detect and quantify retinal vascular permeability changes in a small animal model. By injecting an intravascular dye that can act as a wavelength-dependent absorbing contrast agent into the bloodstream of a small animal, retinal vascular permeability changes induced by retinal diseases or external agents directly injected into the vitreous could be measured using spectroscopic OCT. Because OCT enables depth-resolved imaging of the retina, this technique may enable quantitative mapping of vascular permeability *in vivo*, which may have a significant impact on understanding the mechanisms of diseases that alter retinal vascular permeability, such as diabetic retinopathy. In this study, an OCT system with a diffraction-limited small animal imaging interface and a dual-wavelength OCT spectrometer for spectroscopic measurements was designed and built. Using this dual-wavelength spectroscopic OCT system, the rat retina could be imaged at two different wavelength bands simultaneously, and methods for analyzing spectroscopic OCT data were investigated for retinal vascular permeability measurement.

Thesis Supervisor: James G. Fujimoto
Title: Professor of Electrical Engineering and Computer Science

Acknowledgments

I thank my thesis advisor Professor Jim Fujimoto for all the guidance and resources he provided to complete this thesis. His keen insight and experience in optics and biomedical instrumentations have been especially helpful. The opportunity to have worked with him will always be highly appreciated.

I also want to thank all my colleagues in the Laser Medicine and Medical Imaging Group at MIT. In particular, I would like to thank Dr. Bernhard Baumann for being a wonderful friend as well as an for being an exceptional mentor. This work could not have been so enjoyable without the help and guidance from him.

Drs. Edward Feener and Allen Clermont at Joslin Diabetes Center also provided their time and expertise to support this work. Their knowledge in small animal disease models was essential for this study.

Finally, I would like to thank my family for their unconditional support.

Table of Contents

Chapter 1

Introduction and Background

1.1 Introduction

Increased retinal vascular permeability or blood-retinal barrier breakdown due to diabetes can cause proliferative diabetic retinopathy and diabetic macular edema, which are one of the leading causes of vision loss in developed countries [1, 2]. Therefore, animal models with increased retinal vascular permeability and methods to quantitate this condition are critical to understanding the mechanisms of the disease as well as developing treatments of it. Although there are methods to quantitate retinal vascular permeability, they typically require enucleation of the eye followed by labor intensive sample preparation steps, and it has been difficult to quantitatively assess retinal vascular permeability *in vivo*. Quantitative measurement of retinal vascular permeability *in vivo* is expected to provide potentially more information than conventional methods and facilitate large scale studies. Moreover, *in vivo* measurements can enable time progression studies since they do not require sacrificing the animal. Therefore, in evaluating agents for treatment of diabetic macular edema in humans, a convenient method to quantitate retinal vascular permeability *in vivo* in appropriate animal models is highly desired.

1.2 Background

Measurement of Retinal Vascular Permeability

Evans blue (EB) is a standard intravascular dye used for characterization of blood-retinal barrier breakdown in small animal models [3-5]. EB has an important property that it strongly binds to the blood plasma protein albumin. Because of this property, whenever blood plasma extravasates from blood vessels, the albumin-dye complex exudes into surrounding tissue as well [6]. Therefore EB can be used to assess vascular permeability changes in small animals.

Conventionally, spectrophotometry and fluorescence imaging have been used for measuring vascular permeability in small animal models [7, 8]. In the spectrophotometry method, EB is injected into the bloodstream of the small animal, so that the albumin-dye complex leaks into surrounding tissues when plasma extravasates from blood vessels. After a circulation time of a few hours, the animal is sacrificed and perfused with saline in order to clear the EB in the blood stream. The eye is then enucleated and the retina is isolated from the rest of the eye. The extravasated EB dye can be extracted from retinal tissue using solvents such as formamide. Its concentration in the solvent can then be measured with spectrophotometry to determine the total extravasated amount of EB. In fluorescence imaging, a fluorescence dye, such as indocyanine green (ICG) or fluorescein, is injected into the bloodstream instead, and fluorescence imaging is directly performed *in vivo* or the retinal flat mount technique is used prior to fluorescence imaging for more accurate measurement.

The conventional methods for measuring vascular permeability have a few major drawbacks. The spectrophotometric method can only measure the total quantity of the EB-albumin compounds extravasated out of the retinal vasculature, and therefore cannot provide information about the local leakage sites across the retina and their severity. The fluorescence imaging method can provide information about the local leakage sites across the retina, but is qualitative and quantitative measurement is difficult. Furthermore, the spectrophotometric method and the retinal flat mount technique require enucleation of the eye and fixation of the retina. This process is time consuming and labor intensive. Therefore, a technique that enables quantitative measurement *in situ*, without the need to remove or process specimens, is desirable.

In this thesis, optical coherence tomography (OCT), a diagnostic tool which can perform non-contact, non-invasive, real-time, cross-sectional imaging of the retina and anterior eye, will be used to quantify thicknesses of intraretinal layers and extract information about the extent and location of retinal vascular permeability changes using spectroscopic methods. Spectroscopic OCT using Evans blue as an absorbing contrast agent promises to overcome the limitations of the conventional methods, enabling *in situ* measurement of changes in vascular permeability, without the need to remove or process specimens. Since OCT has become a clinical standard for quantifying diabetic macular edema in humans, it is therefore the preferred method in animal

models as well.

Previous work has shown that intravitreal injection of carbonic anhydrase I (CA-I) in rats alters retinal pH regulation leading to changes in retinal vascular permeability [7]. In this thesis, an animal model with increased retinal vascular permeability will be generated by intravitreal injection of carbonic anhydrase I.

Optical Coherence Tomography

Optical coherence tomography (OCT) is a non-invasive, non-contact biomedical imaging technology that can perform real-time tomographic imaging of biological tissue *in vivo* with a micron-scale resolution [9]. OCT imaging is analogous to ultrasound imaging in that OCT measures the backreflected or backscattered light while ultrasound imaging measures acoustic waves. OCT has been shown to be a particularly useful technology for biological imaging [10, 11]. Changes in tissue properties lead to changes in backscattered light from different layers of biological tissue and alter architectural morphology measured by OCT imaging. Previous studies have demonstrated that these changes associated with early disease can be identified with OCT [12-15]. Because OCT is compatible with fiber optics, OCT sample probe can be designed in diverse ways, thereby allowing adaptation of the technology to a wide range of instruments including ophthalmoscopes, small endoscopes, catheters, probes, needles, or other surgical instruments.

One of the main advantages using OCT in this thesis for measuring retinal vascular permeability is that OCT enables real-time, *in vivo* measurement of back-scattered light from different layers of biological tissue, and therefore, it is not necessary to enucleate and process the rat eye as required in the conventional spectrophotometric and fluorescence imaging methods. Since OCT can measure depth-dependent back-scattered light intensity with superior axial resolutions between 1 and 15 microns [16-20], OCT is well suited for spectroscopic detection [21, 22] of changes in absorption coefficient using the Beer-Lambert law, which describes the change in light intensity as it travels through an optical medium.

1.3 Scope of Thesis

The objective of this thesis is to develop a dual-wavelength spectroscopic OCT technique to measure retinal vascular permeability changes in small animals. By injecting EB dye into the bloodstream of a small animal model, retinal vascular permeability changes induced by CA-I could be measured using spectroscopic OCT. Combined with depth-resolved imaging enabled by OCT, this technique may enable quantitative mapping of vascular permeability measurements *in vivo*. Quantitative measurements of blood-tissue barrier breakdown *in vivo* may have a significant impact on understanding the mechanisms of diseases that alter vascular permeability, such as diabetic retinopathy.

Chapter 2 discusses the theory of spectral / Fourier domain OCT. Theoretical models of spectral / Fourier domain OCT imaging of a single reflector and biological tissue are derived and discussed. The imaging range, axial resolution, and sensitivity roll-off of spectral / Fourier domain OCT is described. Issues related to interference spectrum recalibration and signal processing required for optimal image quality are discussed. Noise and sensitivity in spectral / Fourier OCT is analyzed. Finally, the speckle phenomenon in OCT is discussed.

Chapter 3 discusses the spectroscopic OCT system design. A feasibility analysis for *in vivo* measurement of changes in vascular permeability is provided to determine which light sources can be used for the spectroscopic OCT system. A detailed description of the dual-wavelength spectroscopic OCT system, including its light sources, interferometer, reference arm, imaging interface, and spectrometer, is provided. The software used in image acquisition and important signal processing issues specifically related to the dual-wavelength configuration are described. Finally, the performance of the system is summarized.

Chapter 4 demonstrates spectroscopic imaging and data analysis for measuring retinal vascular permeability changes in small animal models. Animal procedures used in this study are described. Data processing methods for spectroscopic analysis are discussed. Preliminary results demonstrating wavelength-dependency of the OCT signal in the presence of Evans blue dye are shown, and future directions for the study are summarized.

References

1. R. Williams, M. Airey, H. Baxter, J. Forrester, T. Kennedy-Martin, and A. Girach, "Epidemiology of diabetic retinopathy and macular oedema: a systematic review," Eye **18**, 963-983 (2004).
2. J. H. Kempen, B. J. O'Colmam, C. Leske, S. M. Haffner, R. Klein, S. E. Moss, H. R. Taylor, R. F. Hamman, S. K. West, J. J. Wang, N. G. Congdon, D. S. Friedman, and G. Eye Dis Prevalence Res, "The prevalence of diabetic retinopathy among adults in the United States," Arch. Ophthalmol. **122**, 552-563 (2004).
3. Q. W. Xu, T. Qaum, and A. P. Adamis, "Sensitive blood-retinal barrier breakdown quantitation using Evans blue," Invest. Ophthalmol. Vis. Sci. **42**, 789-794 (2001).
4. D. Skondra, K. Noda, L. Almulki, F. Tayyari, S. Frimmel, T. Nakazawa, I. K. Kim, S. Zandi, K. L. Thomas, J. W. Miller, E. S. Gragoudas, and A. Hafezi-Moghadam, "Characterization of azurocidin as a permeability factor in the retina: Involvement in VEGF-induced and early diabetic blood-retinal barrier breakdown," Invest. Ophthalmol. Vis. Sci. **49**, 726-731 (2008).
5. A. Saria and J. M. Lundberg, "Evans blue fluorescence - quantitative and morphological evaluation of vascular permeability in animal tissues," J. Neurosci. Methods **8**, 41-49 (1983).
6. T. Okamura, N. Ishibashi, T. S. Kumar, D. Zurakowski, Y. Iwata, H. G. W. Lidov, and R. A. Jonas, "Hypothermic Circulatory Arrest Increases Permeability of the Blood Brain Barrier in Watershed Areas," Ann. Thorac. Surg. **90**, 2001-2008 (2010).
7. B. B. Gao, A. Clermont, S. Rook, S. J. Fonda, V. J. Srinivasan, M. Wojtkowski, J. G. Fujimoto, R. L. Avery, P. G. Arrigg, S. E. Bursell, L. P. Aiello, and E. P. Feener, "Extracellular carbonic anhydrase mediates hemorrhagic retinal and cerebral vascular permeability through prekallikrein activation," Nat. Med. **13**, 181-188 (2007).
8. T. Ito, T. Itoshima, M. Ukida, S. Kiyotoshi, K. Kawaguchi, H. Ogawa, M. Kitadai, S. Hattori, S. Mizutani, and K. Kita, "Peritoneoscopy of the liver stained by intravenous injection of indocyanine green-experimental and clinical studies," Gastroenterologia Japonica **18**, 593-598 (1983).
9. D. Huang, E. A. Swanson, C. P. Lin, J. S. Schuman, W. G. Stinson, W. Chang, M. R. Hee, T. Flotte, K. Gregory, C. A. Puliafito, and J. G. Fujimoto, "Optical Coherence Tomography," Science **254**, 1178-1181 (1991).
10. W. Drexler and J. Fujimoto, eds., *Optical Coherence Tomography: Technology and Applications* (Biological and Medical Physics, Biomedical Engineering) (Springer, 2008).
11. A. F. Fercher, W. Drexler, C. K. Hitzenberger, and T. Lasser, "Optical coherence tomography-principles and applications," Reports on Progress in Physics **66**, 239-303 (2003).
12. W. Drexler, H. Sattmann, B. Hermann, T. H. Ko, M. Stur, A. Unterhuber, C. Scholda, O. Findl, M. Wirtitsch, J. G. Fujimoto, and A. F. Fercher, "Enhanced visualization of macular pathology with the use of ultrahigh-resolution optical coherence tomography," Archives of Ophthalmology **121**, 695-706 (2003).
13. J. G. Fujimoto, "Optical coherence tomography for ultrahigh resolution in vivo imaging," Nature Biotechnology **21**, 1361-1367 (2003).
14. W. Drexler, "Ultrahigh-resolution optical coherence tomography," Journal of Biomedical

Optics **9**, 47-74 (2004).

15. B. Bouma, G. J. Tearney, S. A. Boppart, M. R. Hee, M. E. Brezinski, and J. G. Fujimoto, "High-resolution optical coherence tomographic imaging using a mode-locked Ti:Al2O3 laser source," Optics Letters **20**, 1486-1488 (1995).
16. W. Drexler, U. Morgner, R. K. Ghanta, F. X. Kärtner, J. S. Schuman, and J. G. Fujimoto, "Ultrahigh-resolution ophthalmic optical coherence tomography," Nature Medicine **7**, 502-507 (2001).
17. B. Povazay, K. Bizheva, A. Unterhuber, B. Hermann, H. Sattmann, A. F. Fercher, W. Drexler, A. Apolonski, W. J. Wadsworth, J. C. Knight, P. S. J. Russell, M. Vetterlein, and E. Scherzer, "Submicrometer axial resolution optical coherence tomography," Optics Letters **27**, 1800-1802 (2002).
18. B. Cense, N. Nassif, T. C. Chen, M. C. Pierce, S. Yun, B. H. Park, B. Bouma, G. Tearney, and J. F. de Boer, "Ultrahigh-resolution high-speed retinal imaging using spectral-domain optical coherence tomography," Optics Express **12**, 2435-2447 (2004).
19. R. A. Leitgeb, W. Drexler, A. Unterhuber, B. Hermann, T. Bajraszewski, T. Le, A. Stingl, and A. F. Fercher, "Ultrahigh resolution Fourier domain optical coherence tomography," Optics Express **12**, 2156-2165 (2004).
20. M. Wojtkowski, V. J. Srinivasan, T. H. Ko, J. G. Fujimoto, A. Kowalczyk, and J. S. Duker, "Ultrahigh-resolution, high-speed, Fourier domain optical coherence tomography and methods for dispersion compensation," Optics Express **12**, 2404-2422 (2004).
21. U. Morgner, W. Drexler, F. X. Kartner, X. D. Li, C. Pitris, E. P. Ippen, and J. G. Fujimoto, "Spectroscopic optical coherence tomography," Optics Letters **25**, 111-113 (2000).
22. D. L. Faber, E. G. Mik, M. C. G. Aalders, and T. G. van Leeuwen, "Light absorption of (oxy-)hemoglobin assessed by spectroscopic optical coherence tomography," Optics Letters **28**, 1436-1438 (2003).

Chapter 2

Spectral / Fourier Domain OCT Theory

2.1 Michelson Interferometer

A typical OCT system can be considered as a Michelson interferometer that is composed of a broadband light source, beamsplitter, reference mirror, sample, and detector. A standard Michelson interferometer with a mirror in the sample arm is shown in Figure 2-1. The beamsplitter in the interferometer divides the light from the broadband light source into two separate beams. Each of the beams, after it is reflected by either the reference or sample mirror, is split once again when it reaches the beamsplitter for the second time. The reference and sample mirrors are located L_R and L_S away from the beamsplitter, respectively. Finally, the two beams that travel to the detector arm interfere with each other at the detector.

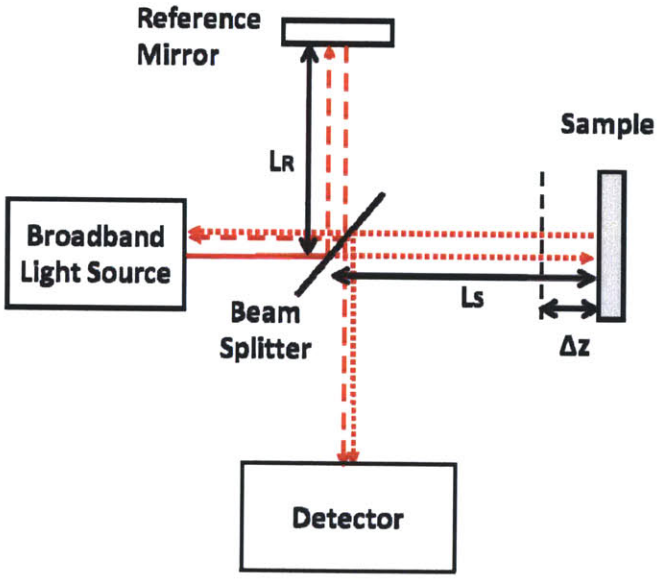

Figure 2-1. The Michelson interferometer composed of a broadband light source, beamsplitter, reference mirror, sample, and detector. The optical path length difference between the sample and reference mirror is $\Delta z \equiv L_S - L_R$.

Before the beam gets split by the beamsplitter, the input complex electric field at the beamsplitter can be expressed as:

$$\boldsymbol{E}(k) = E(k)e^{j\theta(k)} \tag{2.1.1}$$

where $E(k)$ and $\theta(k)$ are the amplitude and phase of the complex electric field at wavenumber k, respectively. In this chapter, boldface variables indicate complex quantities. It should be noted that the phase of the input complex field in general cannot be measured by a simple Michelson interferometer as the detector can measure only the intensity, not the field.

Mathematically, the sum of the fields at the detector at a given optical frequency can be expressed as:

$$\boldsymbol{E}_{tot} = \boldsymbol{E}_R + \boldsymbol{E}_S \tag{2.1.2}$$

where $\boldsymbol{E}_R$ and $\boldsymbol{E}_S$ are the electric fields from the reference and sample mirrors, respectively.

Because the two beams separated by the beamsplitter travel different optical paths, the sum of the fields at the detector at a given optical frequency, or equivalently, at a given wavenumber k can be rewritten as:

$$\boldsymbol{E}_{tot}(k) = \frac{1}{2}\left\{\boldsymbol{r}_R(k)\boldsymbol{E}(k)e^{j2kL_R} + \boldsymbol{r}_S(k)\boldsymbol{E}(k)e^{j2kL_S}\right\} \tag{2.1.3}$$

where $\boldsymbol{r}_R(k)$ and $\boldsymbol{r}_S(k)$ are complex field reflectivities of the reference and sample mirrors, respectively. The factors of 2 in the exponential kernels account for the round-trip propagation in the sample and reference arms of the interferometer. The factor of 2 in the denominator accounts for the power splitting ratio of the beamsplitter.

Because the detector current is proportional to the total intensity, the detector current $I_D(k)$ as a

function of wavenumber can be written as:

$$I_D(k) = \rho(k)\left|\boldsymbol{E}_{tot}(k)\right|^2 = \frac{1}{4}\rho(k)\left|E(k)\right|^2\left[R_R(k) + R_S(k) + 2\,\mathrm{Re}\{\boldsymbol{r}_R^{\,*}(k)\boldsymbol{r}_S(k)e^{j2k\Delta z}\}\right] \quad (2.1.4)$$

where $R_R(k) = \left|\boldsymbol{r}_R(k)\right|^2$ and $R_S(k) = \left|\boldsymbol{r}_S(k)\right|^2$ are power reflectivities of the reference and sample mirrors, respectively, and $\Delta z = L_S - L_R$ is the optical path length difference between the reference and sample arms. $\rho(k)$ is the detector responsivity as a function of wavenumber.

2.2 Spectral / Fourier Domain OCT

In spectral / Fourier domain OCT, the detector used in the Michelson interferometer is a spectrometer which can generate a detector current as a function of wavelength. A typical spectrometer for a Michelson interferometer consists of a collimating lens, diffraction grating, focusing lens, and high-speed CCD or CMOS line scan camera as shown in Figure 2-2.

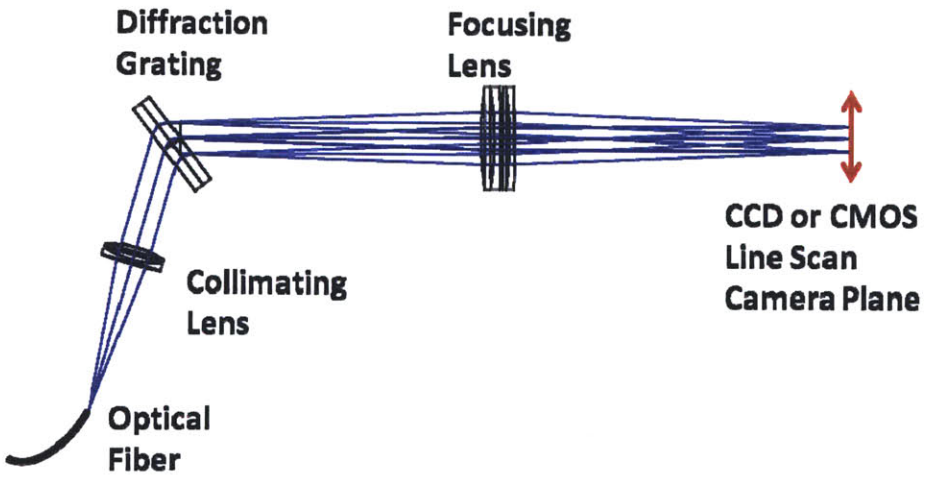

Figure 2-2. Schematic of a spectrometer for spectral / Fourier domain OCT. The spectrometer consists of a collimating lens, diffraction grating, focusing lens, and a high-speed CCD or CMOS line scan camera.

The diffraction grating and focusing lens in the spectrometer focus light at different wavelengths onto different pixels of the CCD or CMOS line scan camera, thereby enabling intensity measurement as a function of wavelength. Therefore, Equation (2.1.4) correctly describes the detector current as a function of wavelength or wavenumber for a single reflector in spectral / Fourier domain OCT.

Single Reflector

If $r_R(k) = 1$ and $r_S(k) = 1$ in Equation (2.1.4) for simplicity, the expression for the detector current can be rewritten as:

$$I_D(k) = \frac{1}{2}\rho(k)\left|E(k)\right|^2 \left\{1 + \cos(2k\Delta z)\right\} \tag{2.2.1}$$

The expression for the detector current in Equation (2.2.1) has a sinusoidal component whose frequency is proportional to the optical path length difference Δz. A peak whose location is linearly proportional to Δz can be obtained by taking the Fourier transform of the expression in Equation (2.2.1) in the case where there is a single reflector in the sample arm. This is illustrated in Figure 2-3.

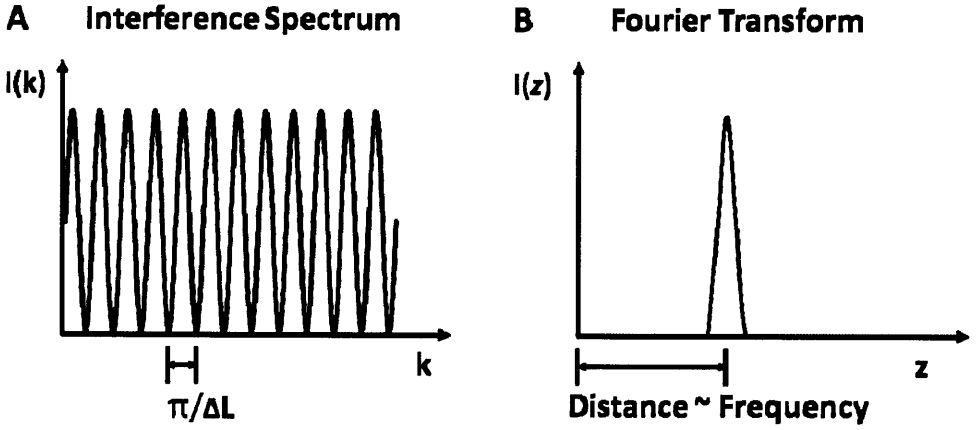

Figure 2-3. (A) An interference spectrum of spectral / Fourier domain OCT for a single reflector in the sample arm. (B) The Fourier transform of the interference spectrum with respect to wavenumber k. The location of the peak is linearly proportional to the optical path length difference Δz.

Therefore, in the Fourier domain, or equivalently, in the z-domain by defining z as the Fourier conjugate variable of k, the location of the peak that corresponds to the frequency of the interference spectrum provides information about the position of the single reflector in the sample arm.

Biological Tissue

A spectral / Fourier domain OCT system can also be built using fiber optics instead of bulk optics as shown in Figure 2-4. In this case, z_R and z_S is the location of the reference mirror and the depth coordinate in the sample arm in terms of the optical path length, respectively. The coupling ratio of the optical coupler is assumed to be 50:50 for the following analysis although it can be different depending on application.

If the sample has many reflecting or backscattering layers as in biological tissue as shown in Figure 2-4, a more careful analysis than in the case of a single reflector in the sample arm is required.

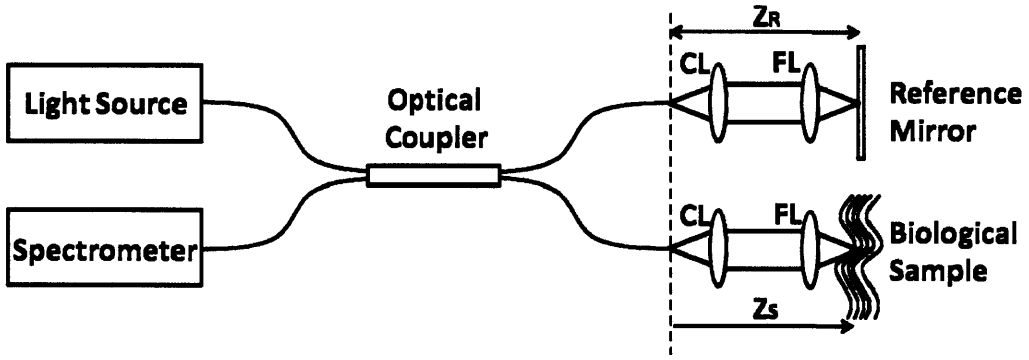

Figure 2-4. A fiber-based spectral / Fourier domain OCT system. The optical coupler replaces a bulk Michelson interferometer. CL: collimating lens, FL: focusing lens.

Analogously to the bulk Michelson interferometer case, the input field to the sample immediately after the fiber tip of the optical coupler in the sample arm is given as:

$$\boldsymbol{E}_i(k) = \frac{1}{\sqrt{2}}\boldsymbol{E}(k)e^{jkL_f} = \frac{1}{\sqrt{2}}E(k)e^{j\theta(k)}e^{jkL_f} \tag{2.2.2}$$

where L_f is the optical path length of the sample arm fiber and $\boldsymbol{E}(k)$ is the complex electric field at the optical coupler before the light is split.

The expression for the input field to the reference arm is the same as above.

For a sample more complicated than a single reflector such as biological tissue, the sample field reflectivity is a function of wavelength and depth:

$$\boldsymbol{r_S} = \boldsymbol{r_S}(k, z_S) = r_S(k, z_S)e^{j\theta_S(k, z_S)} \tag{2.2.3}$$

where $r_S(k,z)$ and $\theta_S(k,z)$ are the magnitude and phase of the sample field reflectivity as a function of depth and wavelength.

The electric field from the reference arm at the detector can be expressed as:

$$\boldsymbol{E}_R(k) = \frac{1}{2}\boldsymbol{r_R}(k)\boldsymbol{E}(k)e^{j2kz_R} \tag{2.2.4}$$

where $\boldsymbol{r_R}(k)$ and z_R are the complex field reflectivity of the reference mirror and the location of the reference mirror, respectively. The common complex exponential terms corresponding to the travel within the fibers are neglected because they exist in both the reference and sample fields and do not affect the intensity at the detector.

Since the sample reflectivity is a function of depth for biological tissue, the electric field from the sample arm at the detector is provided in an integral form:

$$\boldsymbol{E}_S(k) = \frac{1}{2}\int_{-\infty}^{+\infty}\boldsymbol{r_S}(k, z_S)\boldsymbol{E}(k)e^{j2kz_S}dz_S \tag{2.2.5}$$

where $\boldsymbol{r}_S(k, z_S)$ and z_S are the complex field reflectivity of the sample as a function of depth and the depth coordinate in the sample arm, respectively.

Therefore, the total complex electric field at the detector can be expressed as:

$$\boldsymbol{E}_{tot}(k) = \boldsymbol{E}_R(k) + \boldsymbol{E}_S(k) = \frac{1}{2}\boldsymbol{E}(k)\left\{\boldsymbol{r}_R(k)e^{j2kz_R} + \int_{-\infty}^{+\infty}\boldsymbol{r}_S(k, z_S)e^{j2kz_S}dz_S\right\} \tag{2.2.6}$$

For mathematical convenience, the complex exponential term e^{j2kz_R} can be factored out to express all distances in optical path length differences:

$$\boldsymbol{E}_{tot}(k) = \frac{1}{2}\boldsymbol{E}(k)e^{j2kz_R}\left\{\boldsymbol{r}_R(k) + \int_{-\infty}^{+\infty}\boldsymbol{r}'_S(k, \Delta z)e^{j2k\Delta z}d\Delta z\right\} \tag{2.2.7}$$

where $\Delta z = z_S - z_R$ and $\boldsymbol{r}'_S(k, \Delta z) = \boldsymbol{r}_S(k, z_R + \Delta z) = \boldsymbol{r}_S(k, z_S)$.

The detector current can be written as:

$$\begin{aligned} I_D(k) &= \rho(k)\left|\boldsymbol{E}_{tot}(k)\right|^2 \\ &= \frac{1}{4}\rho(k)S(k)\left|\boldsymbol{r}_R(k) + \int_{-\infty}^{+\infty}\boldsymbol{r}'_S(k, \Delta z)e^{j2k\Delta z}d\Delta z\right|^2 \\ &= \frac{1}{4}\rho(k)S(k)\left[R_R(k) + \left|\int_{-\infty}^{+\infty}\boldsymbol{r}'_S(k, \Delta z)e^{j2k\Delta z}d\Delta z\right|^2 + 2\,\mathrm{Re}\left\{\boldsymbol{r}_R^*(k)\int_{-\infty}^{+\infty}\boldsymbol{r}'_S(k, \Delta z)e^{j2k\Delta z}d\Delta z\right\}\right] \end{aligned} \tag{2.2.8}$$

where $S(k) \equiv \left|\boldsymbol{E}(k)\right|^2$, $\rho(k)$, and $R_R(k) \equiv \left|\boldsymbol{r}_R(k)\right|^2$ are the optical power spectrum of the broadband light source, the detector responsivity as a function of wavenumber, and the power reflectivity of the reference mirror.

For biological tissue, the sample reflectivity is typically much smaller than the reference mirror reflectivity, and the reference field typically dominates the sample field. Therefore, the detector current can be rewritten as:

$$\begin{aligned} I_D(k) &\simeq \frac{1}{4}\rho(k)S(k)\left[R_R(k)+2\,\mathrm{Re}\left\{\boldsymbol{r_R}^*(k)\int_{-\infty}^{+\infty}\boldsymbol{r'}_S(k,\Delta z)e^{j2k\Delta z}d\Delta z\right\}\right] \\ &= \frac{1}{4}\rho(k)S(k)R_R(k)+\frac{1}{2}\rho(k)S(k)\sqrt{R_R(k)}\int_{-\infty}^{+\infty}r'_S(k,\Delta z)\cos\left\{2k\Delta z+\Delta\theta(k,\Delta z)\right\}d\Delta z \end{aligned} \tag{2.2.9}$$

where $r'_S(k,\Delta z)$ is the magnitude of $\boldsymbol{r'}_S(k,\Delta z)$ and $\Delta\theta(k,\Delta z)=\theta_S(k,\Delta z)-\theta_R(k)$ is the difference between the phase of the reference mirror field reflectivity and the phase of the sample field reflectivity as a function of depth.

The first term of the interference spectrum in Equation (2.2.9) is commonly referred to as the DC component while the second term is commonly referred to as the AC component as the latter is modulated by sinusoids in the wavenumber domain. As can be seen, it is the AC component that contains information about the sample field reflectivity as a function of depth.

Assuming that $r'_S(k,\Delta z)=r'_S(\Delta z)$ and $\Delta\theta(k,\Delta z)=\Delta\theta(\Delta z)$, which are determined by the magnitude and phase of the sample field reflectivity, are not wavelength-dependent for simplicity, the Fourier transform of the detector current can be expressed as:

$$\begin{aligned} \widetilde{I_D}(z) &= \mathbb{F}\{I_D(k)\} \\ &= \frac{1}{4}\zeta(z)+\frac{\pi}{2}\xi(z)\otimes\int_{-\infty}^{+\infty}r'_S(\Delta z)\left\{e^{-j\Delta\theta(\Delta z)}\delta(z-2\Delta z)+e^{j\Delta\theta(\Delta z)}\delta(z+2\Delta z)\right\}d\Delta z \\ &= \frac{1}{4}\zeta(z)+\frac{\pi}{2}\int_{-\infty}^{+\infty}r'_S(\Delta z)\left\{e^{-j\Delta\theta(\Delta z)}\xi(z-2\Delta z)+e^{j\Delta\theta(\Delta z)}\xi(z+2\Delta z)\right\}d\Delta z \end{aligned} \tag{2.2.10}$$

where $\zeta(z)\equiv\mathbb{F}\left\{\rho(k)S(k)R_R(k)\right\}$, $\xi(z)\equiv\mathbb{F}\left\{\rho(k)S(k)\sqrt{R_R(k)}\right\}$, and $\otimes$ denotes convolution.

The Fourier transform of the detector current can be rewritten in a more informative form as:

$$\widetilde{I_D}(z) = \frac{1}{4}\zeta(z) + \frac{\pi}{2}\int_{-\infty}^{+\infty} e^{-j\Delta\theta(\Delta z)} r'_S(\Delta z)\xi(z-2\Delta z)d\Delta z + \frac{\pi}{2}\int_{-\infty}^{+\infty} e^{j\Delta\theta(\Delta z)} r'_S(\Delta z)\xi(z+2\Delta z)d\Delta z \qquad (2.2.11)$$

Equation (2.2.11) summarizes several important characteristics of spectral / Fourier domain OCT. $\frac{1}{4}\zeta(z)$, which is the Fourier transform of $\rho(k)S(k)R_R(k)$, is the DC component. Because in most cases $\rho(k)S(k)R_R(k)$ has negligible modulation as a function of wavenumber when compared to the AC component of the interference spectrum, it appears at the zero frequency or zero delay position in the z -domain.

Note that the last two terms of Equation (2.2.11) are convolution integrals. The depth-dependent complex sample field reflectivity $r'_S(\Delta z)e^{-j\Delta\theta(\Delta z)}$ is convolved with $\xi(z)$. In other words, the Fourier transform of the detector current $\widetilde{I_D}(z)$ provides a blurred image of the sample field reflectivity $r'_S(\Delta z)e^{-j\Delta\theta(\Delta z)}$ where the point spread function is $\xi(z)$, which is determined by $\rho(k)S(k)\sqrt{R_R(k)}$. Therefore, if the point spread function is narrow enough, an image of the sample reflectivity without significant blurring can be generated using spectral / Fourier domain OCT. Typical axial resolutions of OCT are between 1 and 15 microns [1-5].

Note that in the Fourier domain, $\widetilde{I_D}(z)$ is Hermitian symmetric. This is expected because the Fourier transform of an interference spectrum, which is inherently a real-valued signal, is always Hermitian symmetric. In spectral / Fourier domain OCT, Hermitian symmetry implies that a mirror image of the sample reflectivity appears on both sides of the zero delay. This kind of artifact, referred to as complex conjugate artifact in Fourier domain OCT, is not a problem if the sample is located strictly on one side of the zero delay, in which case only one side of the delay needs to be displayed. However, there have been a number of approaches developed to overcome this artifact to extend the total imaging range of spectral / Fourier domain OCT by a factor of two [6-11].

The properties and characteristics of spectral / Fourier domain OCT described above are illustrated in Figure 2-5.

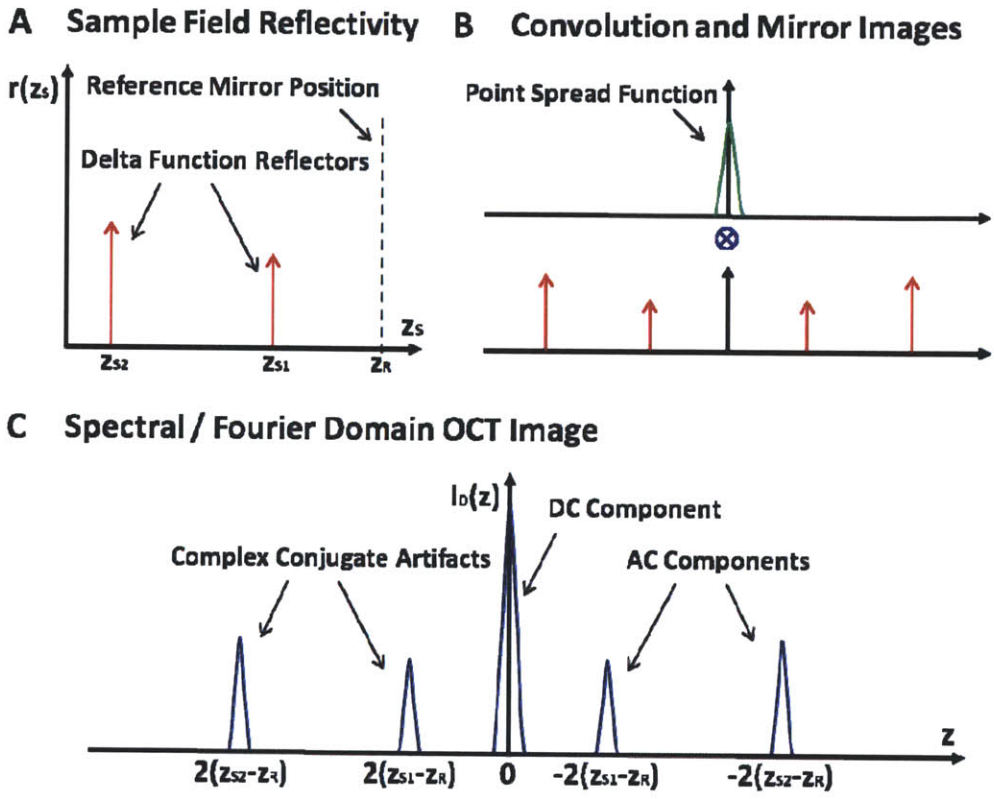

Figure 2-5. (A) Example sample field reflectivity for delta function reflectors. (B) The convolution of the spectral / Fourier domain OCT point spread function and the sample field reflectivity and its complex conjugate mirror image generates (C) the spectral / Fourier domain OCT image. The image is composed of the DC component and complex conjugate artifacts as well as the desired part of the image, which are labeled as the AC components.

2D and 3D Imaging

The previous sections described how an axial scan, or an A-scan, is generated with spectral / Fourier domain OCT. By scanning the sample arm beam in the transverse direction using a

galvanometer scanner while acquiring multiple axial scans sequentially, two-dimensional or three-dimensional spectral / Fourier domain OCT images can be generated. This is illustrated in Figure 2-6. A two-dimensional OCT image, which is a collection of multiple A-scans acquired sequentially while scanning the beam in the transverse direction, is commonly referred to as a B-scan. Only one side of the zero delay is displayed in the OCT image. Due to the recent advancement in the acquisition speed enabled by Fourier domain OCT [12-15], three-dimensional volumetric images can be generated by scanning the beam relatively slowly in one direction as well while acquiring multiple B-scans rapidly in the orthogonal direction.

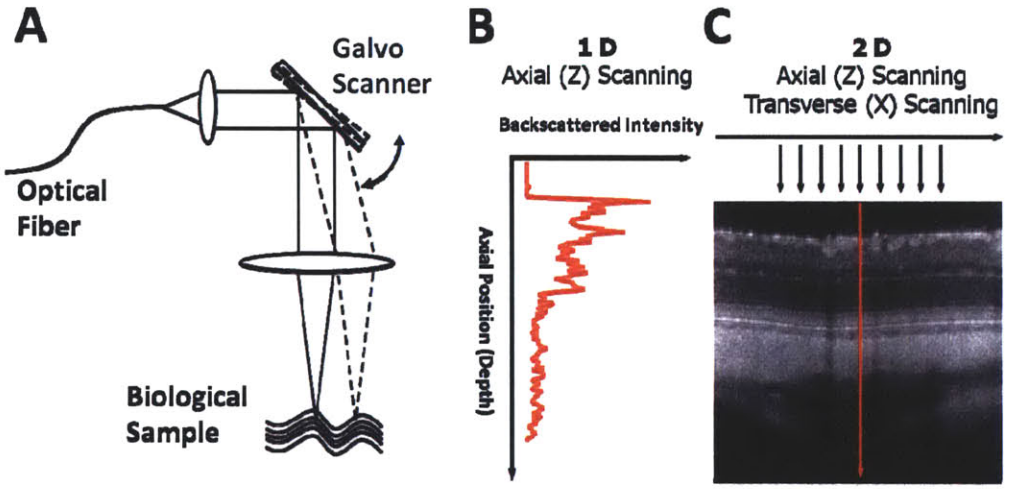

Figure 2-6. (A) A 2D or 3D OCT image is generated by scanning the beam on the sample in the transverse direction. (B) An OCT scan at one transverse position provides an OCT A-scan. (C) Sequential acquisition of OCT A-scans while scanning in the transverse direction allows formation of an OCT B-scan.

Axial Resolution of OCT

As can be seen in Equation (2.2.11), the point spread function of spectral / Fourier domain OCT is given by:

$$\xi(z) \equiv \mathbb{F}\left\{\rho(k)S(k)\sqrt{R_R(k)}\right\} \tag{2.2.12}$$

The detector responsivity as a function of wavenumber $\rho(k)$, the power spectrum of the broadband light source $S(k)$, and the magnitude of the reference mirror field reflectivity $\sqrt{R_R(k)}$ together determine the resolution of an spectral / Fourier domain OCT system. $\sqrt{R_R(k)}$ includes the effect of chromatic aberration of the reference arm optics. Although not explicitly included in the analysis, the collection efficiency of the sample arm optics, which can be wavelength-dependent due to chromatic aberration, also contributes to the resolution in the same way the magnitude of the reference mirror field reflectivity does.

For illustrative purposes, assume that $\beta(k) \equiv \rho(k)S(k)\sqrt{R_R(k)}$ has a normalized Gaussian-shaped spectral distribution:

$$\beta(k) = e^{-\left[\frac{(k-k_0)}{\Delta k}\right]^2} \tag{2.2.13}$$

where k_0 is the central wavenumber of the spectrum $\beta(k)$ and Δk is the spectral bandwidth.

The normalized Gaussian function and its Fourier transform are given by:

$$e^{-\left[\frac{(k-k_0)}{\Delta k}\right]^2} \xleftrightarrow{\mathbb{F}} \Delta k\sqrt{\pi}e^{-\left[\frac{z^2\Delta k^2}{4}\right]} \tag{2.2.14}$$

Therefore, if $\beta(k)$ has a Gaussian spectral distribution, the point spread function of the OCT system is also a Gaussian whose width is determined by the spectral bandwidth Δk of $\beta(k)$.

The resolution of spectral / Fourier domain OCT is typically reported as the full width at half maximum (FWHM) value of its point spread function $\xi(z)$. As can be calculated from Equation (2.2.14), the FWHM of the point spread function in this case is:

$$\Delta z_{FWHM} = \frac{4\sqrt{\ln 2}}{\Delta k} \tag{2.2.15}$$

Taking the derivative of both sides of the relationship $k = 2\pi / \lambda$, and plugging the result into Equation (2.2.15) provides the expression for the FWHM resolution of an OCT system in terms of wavelength as:

$$\Delta z_{FWHM} \simeq \frac{2\sqrt{\ln 2}}{\pi} \frac{\lambda_0^{\,2}}{\Delta\lambda} \simeq 0.44 \frac{\lambda_0^{\,2}}{\Delta\lambda} \tag{2.2.16}$$

where λ_0 and $\Delta\lambda$ are the central wavelength and bandwidth of $\beta(k)$ mapped into the wavelength space. Note that Δk is defined as the half width at $1/e$ of $\beta(k)$, and $\Delta\lambda$ is the corresponding bandwidth, not the entire spectral range.

It is commonly assumed as a ballpark measure that the reference mirror power reflectivity and detector spectral responsivity do not have significant wavelength-dependency, in which case the width of $\beta(k)$ is solely determined by the light source power spectrum. As can be seen from Equation (2.2.16), the resolution of an OCT system becomes better as the center wavelength of the light source gets shorter and the bandwidth broader.

Imaging Range

The imaging range of a spectral / Fourier domain OCT system is determined by the Nyquist sampling theorem because the AC component of the interference spectrum needs to be detected by the spectrometer without aliasing.

If the total number of pixels of the line scan camera of the spectrometer is N and the total spectral range spanned by the line scan camera in wavenumber is ΔK, the difference between the wavenumber values sampled by two neighboring pixels is $\Delta k_{Nyq} = \Delta K / N$. According to the Nyquist sampling theorem, $2\Delta k_{Nyq} z_{max} = \pi$ needs to be satisfied to avoid aliasing. Therefore, the maximum imaging range is given by:

$$z_{max} = \frac{\pi N}{2\Delta K} \simeq \frac{\lambda^2 N}{4\Delta\Lambda} \tag{2.2.17}$$

Note that ΔK and $\Delta\Lambda$ are the entire spectral range spanned by the line scan camera pixels, not the FWHM bandwidth of the light source.

Dispersion Mismatch

It has been assumed so far that there is no dispersion mismatch between the sample and reference arms. However, this assumption usually does not hold because the sample and reference arm optics are different in many cases. The dispersion mismatch results in a distorted point spread function that is broader than the theoretically achievable value in the absence of the dispersion mismatch.

Optical dispersion, by definition, is caused by a frequency- or wavenumber-dependent phase modulation, $\varphi(k)$. Therefore, the interference spectrum in the presence of optical dispersion can be modeled mathematically by modifying Equation (2.2.6) as following:

$$\boldsymbol{E}_{tot}(k) = \frac{1}{2}\boldsymbol{E}(k)\left\{\boldsymbol{r}_R(k)e^{j\{2kz_R+\varphi_R(k)\}} + \int_{-\infty}^{+\infty}\boldsymbol{r}_S(k,z_S)e^{j\{2kz_S+\varphi_S(k)\}}dz_S\right\} \tag{2.2.18}$$

where $\varphi_R(k)$ and $\varphi_S(k)$ are the amounts of optical dispersion in the reference and sample arms, respectively.

If there is any dispersion mismatch so that $\varphi_R(k) \neq \varphi_S(k)$, Equation (2.2.18) becomes:

$$\boldsymbol{E}_{tot}(k) = \frac{1}{2}\boldsymbol{E}(k)e^{j2kz_R}e^{j\varphi_R(k)}\left\{\boldsymbol{r}_R(k) + \int_{-\infty}^{+\infty}\boldsymbol{r'}_S(k,\Delta z)e^{j\{2k\Delta z+\Delta\varphi(k)\}}d\Delta z\right\} \tag{2.2.19}$$

where $\Delta\varphi(k) \equiv \varphi_S(k) - \varphi_R(k)$ is the dispersion mismatch.

Therefore, the resultant interference spectrum in the presence of the dispersion mismatch becomes:

$$I_D(k) = \frac{1}{4}\rho(k)S(k)R_R(k) + \frac{1}{2}\rho(k)S(k)\sqrt{R_R(k)}\int_{-\infty}^{+\infty} r'_S(k,\Delta z)\cos\left\{2k\Delta z + \Delta\theta(k,\Delta z) + \Delta\varphi_{disp}(k)\right\}d\Delta z \quad (2.2.20)$$

Note that in many applications, $\Delta\varphi_{disp}(k)$ is not a function of depth. This fact becomes very useful for system calibration and signal processing purposes.

Spectrometer Roll-off

In reality, the sensitivity of a typical spectral / Fourier domain OCT system drops as the frequency of the interference spectrum becomes higher. There are several factors contributing to this phenomenon.

The rectangular shape of camera pixels results in local averaging of the interference spectrum. Because this local averaging has a low pass filtering effect on the interference spectrum, this results in the depth-dependent signal decay. Similarly, the finite spot size of the focused beam at the camera pixel plane has an additional low pass filtering effect, which also reduces the system sensitivity at deeper depths. Even the diffraction-limited spot size on the line scan camera is usually on the order of ~10 μm, which is comparable to the typical camera pixel size.

Other factors that contribute to spectrometer roll-off include the electronic interpixel crosstalk present in CCD or CMOS detectors, partial aliasing [16], and local fringe visibility loss. Because an OCT spectrometer typically uses a diffraction grating, which results in a spectrum evenly spread in wavelength rather than in wavenumber, camera pixels, which are distributed evenly in space, cannot be mapped linearly to uniformly sampled wavenumber. Since $k = 2\pi/\lambda$, the interference spectrum visibility is reduced at shorter wavelengths first due to the finite spot

size and rectangular pixels, which results in point spread function broadening at deeper depths as well as sensitivity roll-off in depth. Because of the same reason, partial aliasing, which also has a negative effect on sensitivity roll-off, starts happening at shorter wavelengths first near the end of the imaging range.

2.3 System Calibration and Signal Processing

This section discusses system calibration and signal processing required by spectral / Fourier domain OCT in order to achieve optimal image quality.

Hilbert Transformation

As can be seen in Equation (2.2.1), the interference spectrum for a single reflector, if properly calibrated in the wavenumber space, should be the sum of a DC component and an AC component at a single frequency determined by the optical path length difference between the sample reflector and the reference mirror. The Fourier transform of Equation (2.2.1) with respect to k is:

$$\begin{aligned}\mathbb{F}\{I_D(k)\} &= \mathbb{F}\left[\frac{1}{2}\rho(k)|E(k)|^2\{1+\cos(2k\Delta z)\}\right] \\ &= \frac{\pi}{2}\xi(z)\otimes\{2\delta(z)+\delta(z+2\Delta z)+\delta(z-2\Delta z)\}\end{aligned} \tag{2.3.1}$$

where $\xi(z) \equiv \mathbb{F}\{\rho(k)E^2(k)\}$ is the point spread function of spectral / Fourier domain OCT.

By taking the inverse Fourier transform of only the positive frequency component of (2.3.1), or in other words, by zeroing out the negative frequency and DC components before taking the inverse Fourier transform, the resultant signal is:

$$\mathbb{F}^{-1}\left\{\frac{\pi}{2}\xi(z)\otimes\delta(z-2\Delta z)\right\} = \frac{1}{2}\rho(k)|E(k)|^2 e^{j2k\Delta z} \tag{2.3.2}$$

Note that the resultant signal is a complex exponential function in the wavenumber domain, and the phase of the AC component of Equation (2.2.1) as a function of wavenumber k can be extracted by calculating the angle of the phasor of Equation (2.3.2).

It can be shown mathematically that, by going through exactly the same steps, the phase $f(x)$ of the sinusoidal component of any signal in the following form can be extracted using the Hilbert transform:

$$g(x)\left[A_0 + B_0 \cos\{f(x)\}\right] \tag{2.3.3}$$

where $g(x)$ is an arbitrary slowly varying envelope of the sinusoidal component and A_0 and B_0 are constants. $f(x)$ can be any arbitrary function of x.

Spectrum Recalibration

As discussed previously, a typical spectral / Fourier domain OCT spectrometer does not sample the interference spectrum evenly in wavenumber k as desired because the angle of diffraction of the diffraction grating for a given incident angle is linearly proportional to wavelength λ. Instead, the raw interference spectrum acquired by the OCT spectrometer is approximately evenly sampled in wavelength. However, as can be seen from Equations (2.2.1) and (2.2.9), an interference spectrum uniformly sampled in wavenumber k is required for spectral / Fourier domain OCT because the Fourier transform needs to be taken in the wavenumber space to obtain OCT images. Therefore, a numerical recalibration step that maps pixels that are uniformly sampled in wavelength λ to pixels that are uniformly sampled in wavenumber k is required.

In spectral / Fourier domain OCT, it is possible to utilize the fact that the pixel location is linearly proportional to wavelength λ due to the diffraction grating, and use the $k = 2\pi / \lambda$ relationship along with an interpolation method, such as the cubic spline interpolation, to recalibrate the interference spectrum. However, this assumption may not be good enough for quantitative reflectivity measurement because inaccurate spectrum recalibration results in an OCT point

spread function that degrades in shape and width with depth. Therefore, a more accurate recalibration method is necessary.

Note that the spectrometer of spectral / Fourier domain OCT is independent of the rest of the OCT system because the pixel to wavenumber mapping is purely determined by the position of the line scan camera in relative to those of the diffraction grating and the focusing lens of the spectrometer. Therefore, it is possible to use a second Michelson interferometer with equal amounts of dispersion in the sample and reference arms for recalibration purposes only. However, not only it is difficult to build a perfectly balanced Michelson interferometer, but using an additional Michelson interferometer for recalibration requires frequent disconnection of the spectrometer from the OCT system, which is not convenient. For this reason, a recalibration method that can use the existing Michelson interferometer of the OCT system is desired.

From Equation (2.2.20), when there is a single reflector in the sample arm, the phase of the sinusoidal component should be linearly increasing in wavenumber k if there is no dispersion mismatch between the sample and reference arms. However, what actually can be acquired prior to recalibration is the following:

$$I_D[n] = \frac{1}{4}\rho[n]S[n]R_R[n] + \frac{1}{2}\rho[n]S[n]\sqrt{R_R[n]}\cos\left(\varphi_{delay}[n,\Delta z] + \Delta\varphi_{disp}[n]\right) \qquad (2.3.4)$$

where the square brackets denote discretely sampled functions, n is the pixel number, $\Delta\varphi_{disp}[n]$ is the phase due to the dispersion mismatch between the two arms, and $\varphi_{delay}[n,\Delta z]$ is the phase due to the delay between the two arms. Note that $\varphi_{delay}[n,\Delta z] = 2f_{map}[n]\Delta z + \theta_0$ for a single reflector in the sample arm where θ_0 is a constant phase offset, and an accurate one-to-one mapping function $n = f_{map}^{-1}(k)$ between the sample location n and wavenumber k is required for recalibration.

The Hilbert transform can be used on Equation (2.3.4) to extract the phase of the sinusoidal component $\varphi_{delay}[n,\Delta z] + \Delta\varphi_{disp}[n]$. The phase due to the dispersion mismatch is not desired for

interference spectrum recalibration. However, note that $\Delta\varphi_{disp}[n]$ is not a function of Δz while $\varphi_{delay}[n,\Delta z]$ is. Therefore, by acquiring the raw interference spectra at two different delays and taking the difference of the phases, $\Delta\varphi_{disp}[n]$ can be cancelled as following[17]:

$$\varphi_{diff}[n] = \left(\varphi_{delay}[n,2\Delta z] + \Delta\varphi_{disp}[n]\right) - \left(\varphi_{delay}[n,\Delta z] + \Delta\varphi_{disp}[n]\right) = 2f_{map}[n]\Delta z + \Delta\theta \quad (2.3.5)$$

where $\varphi_{delay}[n,\Delta z] = 2f_{map}[n]\Delta z + \theta_0$ and $\varphi_{delay}[n,2\Delta z] = 4f_{map}[n]\Delta z + \theta_1$ were used to obtain the result.

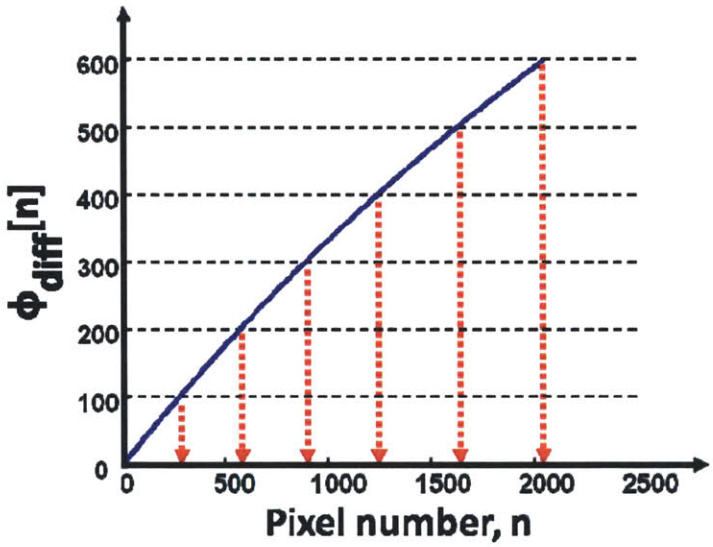

Figure 2-7. Determination of the interpolation locations for interference spectrum recalibration. The locations where interpolation is required to resample the interference spectrum correctly can be identified by evenly dividing the entire phase range with the total number of sample points desired and determining the pixel numbers corresponding to those phase values.

As can be seen from Equation (2.2.20), when there is a single reflector in the sample arm without the dispersion mismatch, the phase difference $\varphi_{diff}[n]$ should be linearly increasing with sample number n, if the interference spectrum is sampled correctly. However, the plot of $\varphi_{diff}[n]$ as a

function of n is usually not a straight line before recalibration, but an arbitrary function determined by the spectrometer configuration. Therefore, to resample the interference spectrum correctly, the raw spectrum needs to be interpolated. The locations where the interference spectrum needs to be interpolated to resample the spectrum correctly can be identified by equally dividing the entire range of the phase difference $\varphi_{diff}[n]$ with the total number of sample points desired and determining the new locations n's corresponding to those phase values. Note that the new n's where interpolation is required are not necessarily integer-valued. This step is graphically demonstrated in Figure 2-7.

Once the new locations n's are determined, a correctly recalibrated version of the interference spectrum can be obtained by interpolating the raw interference spectrum at those locations. The effect of spectrum recalibration on the interference spectrum is simulated in Figure 2-8. Note that the shape of the envelope of the interference spectrum is also affected by recalibration as expected.

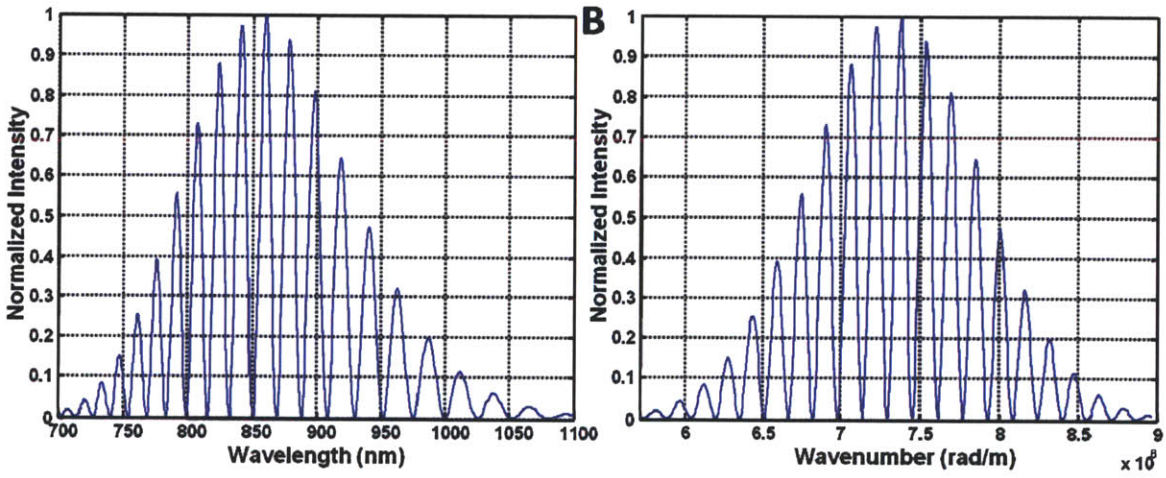

Figure 2-8. The effect of spectrum recalibration on the interference spectrum. (A) An interference spectrum for a single reflector acquired by spectral / Fourier domain OCT. The pixel locations of the spectrometer are assumed to be linear in wavelength. Note that the frequency is lower for longer wavelengths in the wavelength space even though there is only one reflector in the sample arm. (B) A recalibrated version of the interference spectrum shown in (A). Spectrum recalibration results in a single modulation frequency.

Numerical Dispersion Compensation

In OCT, the dispersion mismatch between the sample and reference arms degrades the axial resolution. Physically removing the dispersion mismatch in the Michelson interferometer completely is very difficult, and there is always some amount of residual dispersion mismatch remaining in the system. However, in spectral / Fourier domain OCT, it is possible to compensate for the dispersion mismatch numerically to recover the optimal resolution allowed by the OCT system in the absence of the dispersion mismatch.

Consider multiplying the AC component of Equation (2.2.20) with the complex exponential of the dispersion mismatch $\Delta\varphi_{disp}(k)$.

$$I_{D,AC}(k) = \frac{1}{2}\rho(k)S(k)\sqrt{R_R(k)}e^{j\Delta\varphi_{disp}(k)}\int_{-\infty}^{+\infty} r'_S(k,\Delta z)\cos\left\{2k\Delta z + \Delta\theta(k,\Delta z) + \Delta\varphi_{disp}(k)\right\}d\Delta z \quad (2.3.6)$$

Using Euler's formula, Equation (2.3.6) can be rewritten as:

$$\begin{aligned} I_{D,AC}(k) = {} & \frac{1}{4}\rho(k)S(k)\sqrt{R_R(k)}\int_{-\infty}^{+\infty} r'_S(k,\Delta z)e^{j\left\{2k\Delta z+\Delta\theta(k,\Delta z)+2\Delta\varphi_{disp}(k)\right\}}d\Delta z \\ & + \frac{1}{4}\rho(k)S(k)\sqrt{R_R(k)}\int_{-\infty}^{+\infty} r'_S(k,\Delta z)e^{-j\left\{2k\Delta z+\Delta\theta(k,\Delta z)\right\}}d\Delta z \end{aligned} \quad (2.3.7)$$

Although the first term on the right side of Equation (2.3.7) still has the term $\Delta\varphi_{disp}(k)$ in the complex exponential, the second term is now free of the dispersion mismatch. In the Fourier domain, because the first term is on one side of the zero delay while the second term is on the other side, the spectral / Fourier domain OCT image without the dispersion mismatch can be obtained from the side that corresponds to the second term of Equation (2.3.7). The image quality on other side of the zero delay is clearly degraded even further due to the $2\Delta\varphi_{disp}(k)$ term in the complex exponential. However, since spectral / Fourier domain OCT generates images that are Hermitian symmetric, only one side of the zero delay needs to be displayed.

Therefore, the dispersion mismatch can be compensated numerically by multiplying the interference spectrum of spectral / Fourier domain OCT with the complex exponential of the dispersion mismatch $\Delta\varphi_{disp}(k)$.

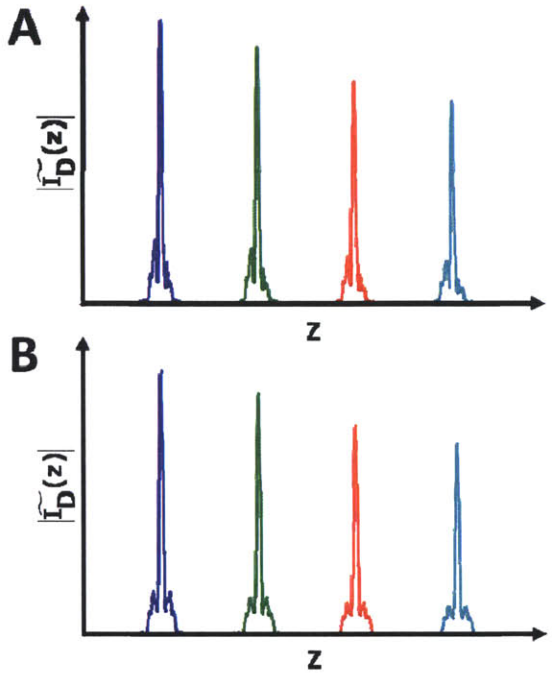

Figure 2-9. (A) Point spread functions at 4 different delays when the dispersion mismatch is not compensated and (B) the corresponding point spread functions when the dispersion mismatch is compensated numerically. The data shown are acquired using an ultrahigh resolution spectral / Fourier domain OCT system and processed in MATLAB.

The effect of dispersion compensation can be clearly seen in Figure 2-9. For a single reflector in the absence of the dispersion mismatch, the shape of the magnitude of the point spread function should be symmetrical about the center of the point spread function regardless of the depth because the point spread function is the Fourier transform of a real-valued signal as shown in Equation (2.2.12). However, if there is any residual dispersion mismatch, the point spread function becomes asymmetric and broader than what it should be because the argument of the sinusoidal term of the interference spectrum is no longer a linearly increasing function in wavenumber. This effect is clearly shown in Figure 2-9. Note that the depth-dependency of the

shape of the point spread function is minimal regardless of the dispersion mismatch, which would not be possible if the interference spectrum were not correctly recalibrated.

In many cases, the amount of the dispersion mismatch $\Delta\varphi_{disp}(k)$ is not known in advance. To date, there have been a few approaches suggested to find the dispersion mismatch caused by biological tissue [3, 5]. One of the approaches is to define an image-sharpness metric, and optimizing it numerically until the sharpest image is obtained according to its definition.

Background Subtraction

In spectral / Fourier domain OCT, the background spectrum, which can be obtained by blocking the sample arm, is typically subtracted from the interference spectrum before taking the Fourier transform. There are several reasons for performing background subtraction.

Firstly, background subtraction eliminates dark current non-uniformity of the CCD or CMOS detector in the spectrometer. Non-uniform dark current results in a fixed pattern, which can be removed by subtracting a reference background spectrum. However, dark current noise, which is a random statistical variation of dark current, is not eliminated by background subtraction.

Secondly, background subtraction is a necessary step for spectral shaping as will be discussed in detail in the next section. By subtracting the reference background spectrum from the OCT interference spectrum, only the AC component of Equation (2.2.9) remains. This AC component can be spectrally shaped before taking the Fourier transform to reduce sidelobes in the point spread function.

Lastly, parasitic reflections can be removed by background subtraction. Because OCT is an interferometric technique, interferences occurring between surfaces other than the sample and reference mirror are also simultaneously embedded in the interference spectrum. Any pair of surfaces in the OCT system, if the optical path length difference is within the imaging range, can create an undesired stationary line in the OCT image when there are parasitic reflections from those surfaces. Since these lines corresponding to parasitic reflections are stationary regardless

of the sample, they can be removed by subtracting the reference background spectrum from the interference spectrum.

Spectral Shaping

As can be seen in Equation (2.2.12), the resolution of spectral / Fourier domain OCT is determined by $\xi(z) \equiv \mathbb{F}\left\{\rho(k)S(k)\sqrt{R_R(k)}\right\}$ where $\rho(k)$, $S(k)$, and $R_R(k)$ are the detector responsivity, power spectrum of the light source, and power back-coupling efficiency of the reference mirror to the detector. In many situations, the optical power spectrum of the light source is the determining factor of the resolution because the detector and the reference mirror are typically chosen based on the light source. However, the detector responsivity and power back-coupling efficiency of the reference mirror can also affect the resolution.

Because the point spread function of spectral / Fourier domain OCT is determined by the Fourier transform of the product $\rho(k)S(k)\sqrt{R_R(k)}$, there can be sidelobes in the point spread function depending on the spectral shape of the product. Since OCT images are commonly displayed in the logarithmic scale, the sidelobes of the point spread function need to be very small compared to the main peak. Typically, sidelobes are tolerable if the ratio of the height of the main peak to that of the sidelobe is bigger than the dynamic range of the OCT image. For example, if the dynamic range of an OCT image is 35 dB, sidelobes of up to -35 dB of the main peak would not degrade the image quality significantly because they will be below the noise level of the image.

In OCT, a Gaussian spectrum is desired for the product $\rho(k)S(k)\sqrt{R_R(k)}$ in order to minimize sidelobes. For broadband light sources, this requirement is usually not satisfied, and the Fourier transform of $\rho(k)S(k)\sqrt{R_R(k)}$ in many cases results in non-negligible sidelobes. However, in spectral Fourier domain OCT, it is possible to shape the spectrum numerically in order to reduce the sidelobes. From Equation (2.2.9), the expression for the interference spectrum after numerical background subtraction is:

$$I_{D,AC}(k) = \frac{1}{2}\rho(k)S(k)\sqrt{R_R(k)}\int_{-\infty}^{+\infty} r'_S(k,\Delta z)\cos\{2k\Delta z + \Delta\theta(k,\Delta z)\}d\Delta z \qquad (2.3.8)$$

Although, strictly speaking, $\rho(k)S(k)\sqrt{R_R(k)} \neq \rho(k)S(k)R_R(k)$, it is reasonable to assume that $R_R(k)$ is approximately wavelength-independent, in which case the ratio of $\rho(k)S(k)\sqrt{R_R(k)}$ to $\rho(k)S(k)R_R(k)$ can be assumed to be constant. Since $\rho(k)S(k)R_R(k)$ is the reference background spectrum, it is possible to divide Equation (2.3.8) with the background spectrum numerically in order to obtain the following interference spectrum:

$$I'_{D,AC}(k) \propto \int_{-\infty}^{+\infty} r'_S(k,\Delta z)\cos\{2k\Delta z + \Delta\theta(k,\Delta z) + \Delta\varphi_{disp}(k)\}d\Delta z \qquad (2.3.9)$$

Finally, by multiplying Equation (2.3.9) with an appropriate spectral shape $V(k)$, an interference spectrum with a desired point spread function $\gamma(z) = \mathbb{F}\{V(k)\}$ can be obtained as following:

$$I''_{D,AC}(k) \propto V(k)\int_{-\infty}^{+\infty} r'_S(k,\Delta z)\cos\{2k\Delta z + \Delta\theta(k,\Delta z) + \Delta\varphi_{disp}(k)\}d\Delta z \qquad (2.3.10)$$

Examples of spectral windows other than the Gaussian include the hyperbolic secant, Hann, Hamming, Blackman, and Kaiser. In determining the window for spectral shaping, both the width of the point spread function and the magnitude of sidelobes should be considered.

Note that there is always a tradeoff between spectral shaping and the signal-to-noise ratio, and it is not possible to improve resolution without degrading the signal-to-noise ratio. This is because the local signal-to-noise ratio varies with wavenumber in the interference spectrum due to, for example, the fact that not all pixels of the line scan camera in the spectrometer are shot noise limited. Noise in spectral / Fourier domain OCT is discussed in detail in the next section.

2.4 Noise and Sensitivity

Sensitivity

An important system parameter in OCT is sensitivity, which is defined as the maximum total attenuation of optical power in the sample arm given that the signal can still be measured. The minimum signal-to-noise ratio required for a signal to be barely measurable is defined as unity.

In OCT, sensitivity is typically measured by putting a mirror in the sample arm. In most cases, a neutral density filter with a known optical density (O.D.) value is inserted in front of the mirror so that the spectrometer is not saturated. According to the definition, the system sensitivity in decibels (dB) can then be calculated as:

$$Sensitivity = 10\log_{10}(SNR) + 20 \times O.D. \tag{2.4.1}$$

where the signal-to-noise ratio SNR is defined in the Fourier domain as the ratio of the magnitude-squared of the peak corresponding to the mirror to the variance of the magnitude of background noise.

Another expression for sensitivity in OCT is in terms of the minimum sample power reflectivity $R_{S,min}$. Because sensitivity is the maximum attenuation in the sample arm given that the signal is barely measurable, it is possible to interpret sensitivity as:

$$Sensitivity = \left.\frac{1}{R_{S,\min}}\right|_{SNR=1} \tag{2.4.2}$$

Sources of Noise

The most fundamental source of noise in OCT is photocurrent noise. It is called shot noise if the incident photons to the detector are Poisson distributed. Shot noise still exists even if the mean optical power P incident on the detector is constant because the number of photons arriving in a

given time interval $T = 1/2B$ is inherently random. For light from an ideal laser with a stable output power, the rate of photon arrivals obeys the Poisson probability distribution. It can be shown that the photocurrent mean and variance are given by:

$$\langle i \rangle = e\eta \frac{P}{h\nu} \tag{2.4.3}$$

$$\sigma_i^2 = 2e\langle i \rangle B \tag{2.4.4}$$

where e, η, h, and ν are the electron charge, quantum efficiency of the detector, Planck constant, and frequency of light.

Therefore, the signal-to-noise ratio of the photocurrent is given by:

$$SNR = \frac{\langle i \rangle^2}{\sigma_i^2} = \frac{\eta P}{2Bh\nu} = \bar{n} \tag{2.4.5}$$

where $\bar{n}$ is the mean photoelectron count during the time interval $T = 1/2B$. In other words, the signal-to-noise ratio of the photoelectric current is directly proportional to the optical power incident on the detector and inversely proportional to the bandwidth of the detector circuit.

Another source of noise is dark current and dark current noise from the detector. Dark current is caused by random generation of electrons and holes even in the absence of light. For a multi-element detector array, the mean of the dark current can vary with pixel, thereby causing a fixed pattern noise which can be removed by background subtraction as discussed previously. However, dark current noise, which is the variance of the dark current shot noise, cannot be removed by background subtraction.

Yet another source of noise is thermal Johnson noise in the detector circuit. It can be shown that the thermal noise current variance for a circuit resistance R is given by:

$$\sigma_i^2 \simeq 4kTB / R \tag{2.4.6}$$

where k and T are the Boltzmann constant and temperature of the circuit, respectively. Thermal noise can be reduced by cooling.

Other sources of noise include excess photon noise and background noise. Excess photon noise arises when there are fluctuations in the optical power of the light source whereas shot noise exists even when the power is constant. However, for spectral / Fourier domain OCT, excess photon noise is typically not an issue. Background noise arises from extraneous photons that reach the detector, and can be removed by covering the spectrometer to block stray light.

Signal-to-Noise Ratio in OCT

Because different sources of noise are not correlated to each other, the variance of the total noise is the sum of the individual variances. However, while the signal always increases linearly with optical power, only the photocurrent variance increases with incident optical power. Therefore, by increasing the incident power to the detector, it is possible to achieve the shot noise limit, where all other sources of noise become negligible compared to shot noise.

In spectral / Fourier domain OCT, a multi-element photo-detector array is used, and it is necessary to analyze the signal-to-noise ratio in the discrete wavenumber domain. Using the discrete Fourier transform for the expression for the point spread function, instead of the continuous time Fourier transform as in Equation (2.2.12), the height of the point spread function is given by :

$$h_{PSF} \equiv \xi(z=0) = \sqrt{R_R} \sum_{m=0}^{N-1} \rho[m] S[m] \tag{2.4.7}$$

where N is the total number of pixels in the line scan camera of the spectrometer. The reference mirror reflectivity is assumed to be wavelength-independent for simplicity.

Because in spectral / Fourier domain OCT, the power from the reference arm dominates that from the sample arm, the shot noise variance from the m^{th} photo-detector is given by:

$$\sigma_i^2[m] = 2eI_D[m]B \simeq \frac{1}{2}eR_R B\rho[m]S[m] \tag{2.4.8}$$

The discrete Fourier transform of an interference spectrum at the zero frequency simply sums the individual sample values together. Because the variance of the sum of uncorrelated variables is the sum of their variances, the variance of noise in the Fourier domain at the zero frequency is therefore the sum of the variances $\sigma_i^2[m]$'s. However, assuming that shot noise is white, the variance at the zero frequency represents the general variance value at all frequencies. Therefore, the noise variance in the Fourier domain in general is given by:

$$\sigma_z^2 = \frac{1}{2}eR_R B\sum_{m=0}^{N-1}\rho[m]S[m] \tag{2.4.9}$$

From Equations (2.2.11) and (2.4.7), the magnitude of the signal in the Fourier domain in the case of a single sample reflector is given by:

$$\left|\tilde{I}_Z(z=\pm 2\Delta z)\right| = \frac{\pi}{2}\sqrt{R_S}\sqrt{R_R}\sum_{m=0}^{N-1}\rho[m]S[m] \tag{2.4.10}$$

Therefore, the signal-to-noise ratio in spectral / Fourier domain OCT is:

$$SNR = \frac{\pi^2}{2}\frac{R_S\sum_{m=0}^{N-1}\rho[m]S[m]}{eB} \tag{2.4.11}$$

Note that the signal-to-noise ratio of spectral / Fourier domain OCT in the shot noise limit increases with the sample power reflectivity, detector responsivity, and optical power, and decreases with the detector bandwidth, which is proportional to the imaging speed.

2.5 Speckle in OCT

A speckle pattern refers to a random intensity fluctuation that occurs in many coherent imaging applications. Although it is still a statistical phenomenon, the speckle effect in OCT imaging of biological tissue is fundamentally different from other sources of noise in OCT in that it does not have a time-dependency as long as the sample is stationary. The speckle effect arises from the interference of a set of waves, and is closely related to the interference effect known as beating. In OCT imaging of biological tissue, the interference of multiple waves occurs when there are multiple scatterers within a single resolution volume determined by the transverse and axial resolutions of OCT.

Mathematically, it is convenient to write the sample field reflectivity as:

$$\boldsymbol{r}'_S(k,\Delta z) = \sum_{m=1}^{N} \boldsymbol{r}_{S,m}(k)\delta(\Delta z - \Delta z_m) \tag{2.5.1}$$

where Δz_m is the optical path length difference between the reference mirror and the location of the m^{th} scatterer in the sample arm. In this case, Equation (2.2.9) can be rewritten as:

$$\begin{aligned} I_D(k) &\simeq \frac{1}{4}\rho(k)S(k)\left[R_R(k) + 2\,\mathrm{Re}\left\{ \boldsymbol{r}_R^{\,*}(k) \int_{-\infty}^{+\infty} \sum_{m=1}^{N} \boldsymbol{r}_{S,m}(k)\delta(\Delta z - \Delta z_m) e^{j2k\Delta z} d\Delta z \right\} \right] \\ &= \frac{1}{4}\rho(k)S(k)R_R(k) + \frac{1}{2}\rho(k)S(k)\sqrt{R_R(k)}\sum_{m=1}^{N} r_{S,m}(k)\cos\left\{2k\Delta z_m + \Delta\theta(k,\Delta z_m)\right\} \end{aligned} \tag{2.5.2}$$

where $r_{S,m}(k)$ is the magnitude of $\boldsymbol{r}_{S,m}(k)$ and $\Delta\theta(k,\Delta z_m)$ is the difference between the phase of the reference mirror field reflectivity and the phase of the sample field reflectivity.

Because of the sum of the multiple frequency components in Equation (2.5.2), an effect analogous to beating can occur if there are multiple scatterers within one resolution volume. As an illustrative example, assume there are two scatterers close to each other. If the two scatterers have equal field reflectivity and the light source emits white light with a flat power spectral

density, the linear superposition of the resulting reflected fields from the two scatterers results in a beating interference spectrum as shown in Figure 2-10.

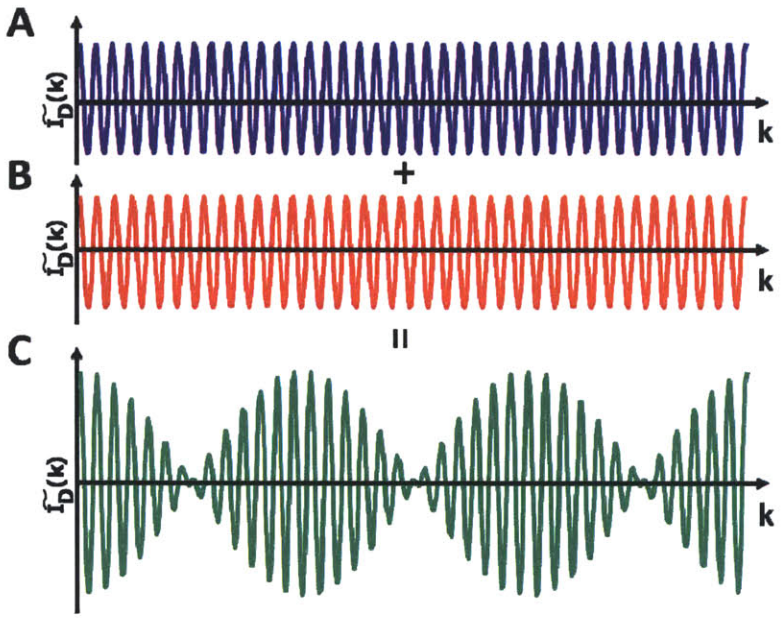

Figure 2-10. Two scatterers close to each other in the sample result in a beating interference spectrum. The beat frequency is the difference between the frequencies of the individual interference spectra in the absence of each other.

If the axial resolution of spectral / Fourier domain were infinitely good, this beating would not result in speckle as the Fourier transform of a beat still exhibits two distinct peaks if the resolution is good enough. However, because of the finite axial resolution of OCT, the entire spectral range of the beat in Figure 2-9 cannot be not detected by the OCT spectrometer. Instead, the beat is modulated by $\rho(k)S(k)\sqrt{R_R(k)}$, which sets the observation window for spectral / Fourier domain OCT. Moreover, because the phase of the beat within the observation window changes when the distance between the two scatterers increases or decreases slightly, the finite axial resolution of OCT may result in an intensity fluctuation at the "mean" position of the two scatterers in the Fourier domain even though the field reflectivities of the two scatterers remain the same. This is illustrated in Figure 2-11.

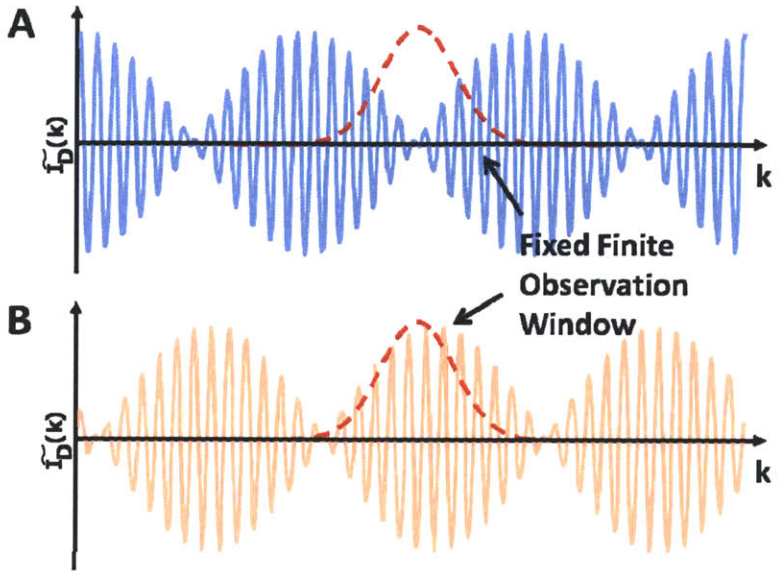

Figure 2-11. The effect of the finite observation window of spectral / Fourier domain OCT on speckle. The finite observation window is determined by the light source, reference mirror reflectivity, and detector responsivity. The difference in the phases of the beats in (A) and (B) result in intensity fluctuation in the Fourier domain.

Because the spatial distribution of scatterers in biological tissue is random even within a macroscopically homogeneous tissue layer, the phase of the beat within the observation window is also inherently random, which makes speckle in OCT a statistical phenomenon. However, note that the resultant speckle pattern is stationary in time as long as the scatterers are stationary as well. In other words, if the same area is scanned multiple times and if the biological tissue of interest is stationary in time, the resultant OCT images have identical speckle patterns.

Although real biological tissue is significantly more complicated than the sample with two scatterers located within one resolution volume of OCT, the nature of the origin of speckle in OCT imaging of biological tissue is essentially the same.

References

1. W. Drexler, U. Morgner, R. K. Ghanta, F. X. Kärtner, J. S. Schuman, and J. G. Fujimoto, "Ultrahigh-resolution ophthalmic optical coherence tomography," Nature Medicine **7**, 502-507 (2001).
2. B. Povazay, K. Bizheva, A. Unterhuber, B. Hermann, H. Sattmann, A. F. Fercher, W. Drexler, A. Apolonski, W. J. Wadsworth, J. C. Knight, P. S. J. Russell, M. Vetterlein, and E. Scherzer, "Submicrometer axial resolution optical coherence tomography," Optics Letters **27**, 1800-1802 (2002).
3. B. Cense, N. Nassif, T. C. Chen, M. C. Pierce, S. Yun, B. H. Park, B. Bouma, G. Tearney, and J. F. de Boer, "Ultrahigh-resolution high-speed retinal imaging using spectral-domain optical coherence tomography," Optics Express **12**, 2435-2447 (2004).
4. R. A. Leitgeb, W. Drexler, A. Unterhuber, B. Hermann, T. Bajraszewski, T. Le, A. Stingl, and A. F. Fercher, "Ultrahigh resolution Fourier domain optical coherence tomography," Optics Express **12**, 2156-2165 (2004).
5. M. Wojtkowski, V. J. Srinivasan, T. H. Ko, J. G. Fujimoto, A. Kowalczyk, and J. S. Duker, "Ultrahigh-resolution, high-speed, Fourier domain optical coherence tomography and methods for dispersion compensation," Optics Express **12**, 2404-2422 (2004).
6. M. Wojtkowski, A. Kowalczyk, R. Leitgeb, and A. F. Fercher, "Full range complex spectral optical coherence tomography technique in eye imaging," Optics Letters **27**, 1415-1417 (2002).
7. J. Zhang, W. Jung, J. S. Nelson, and Z. Chen, "Full range polarization-sensitive Fourier domain optical coherence tomography," Optics Express **12**, 6033-6039 (2004).
8. Y. Yasuno, S. Makita, T. Endo, G. Aoki, M. Itoh, and T. Yatagai, "Simultaneous B-M-mode scanning method for real-time full-range Fourier domain optical coherence tomography," Applied Optics **45**, 1861-1865 (2006).
9. M. V. Sarunic, B. E. Applegate, and J. A. Izatt, "Real-time quadrature projection complex conjugate resolved Fourier domain optical coherence tomography," Optics Letters **31**, 2426-2428 (2006).
10. R. K. K. Wang, "In vivo full range complex Fourier domain optical coherence tomography," Applied Physics Letters **90**, 3 (2007).
11. B. Hofer, B. Povazay, B. Hermann, A. Unterhuber, G. Matz, and W. Drexler, "Dispersion encoded full range frequency domain optical coherence tomography," Optics Express **17**, 7-24 (2009).
12. M. Wojtkowski, R. Leitgeb, A. Kowalczyk, T. Bajraszewski, and A. F. Fercher, "In vivo human retinal imaging by Fourier domain optical coherence tomography," Journal of Biomedical Optics **7**, 457-463 (2002).
13. M. A. Choma, M. V. Sarunic, C. H. Yang, and J. A. Izatt, "Sensitivity advantage of swept source and Fourier domain optical coherence tomography," Optics Express **11**, 2183-2189 (2003).
14. J. F. de Boer, B. Cense, B. H. Park, M. C. Pierce, G. J. Tearney, and B. E. Bouma, "Improved signal-to-noise ratio in spectral-domain compared with time-domain optical coherence tomography," Optics Letters **28**, 2067-2069 (2003).
15. R. Leitgeb, C. K. Hitzenberger, and A. F. Fercher, "Performance of Fourier domain vs. time domain optical coherence tomography," Optics Express **11**, 889-894 (2003).

16. T. Bajraszewski, M. Wojtkowski, M. Szkulmowski, A. Szkulmowska, R. Huber, and A. Kowalczyk, "Improved spectral optical coherence tomography using optical frequency comb," Optics Express **16**, 4163-4176 (2008).
17. S. Makita, T. Fabritius, and Y. Yasuno, "Full-range, high-speed, high-resolution 1-mu m spectral-domain optical coherence tomography using BM-scan for volumetric imaging of the human posterior eye," Optics Express **16**, 8406-8420 (2008).

Chapter 3

Spectroscopic OCT System Design

3.1 Overview

Because of the important properties of Evans blue dye described in Chapter 1, it is desirable to develop a spectroscopic OCT technique that uses Evans blue dye as an absorbing contrast agent to measure vascular permeability changes in small animal models. For this purpose, a dual-wavelength spectroscopic OCT system that enables simultaneous acquisition of OCT images at two different center wavelengths was developed.

The purpose of this chapter is to discuss the dual-wavelength spectroscopic OCT system design. A feasibility analysis for *in vivo* measurement of changes in vascular permeability is provided to determine which light sources can be used. A detailed description of the dual-wavelength spectroscopic OCT system, including its light sources, interferometer, reference arm, imaging interface, and dual-wavelength spectrometer, is followed. The software used for image acquisition and important signal processing issues specifically related to the dual-wavelength configuration are discussed. Finally, the performance of the system is summarized. Dr. Bernhard Baumann from our group collaborated in designing and building the spectroscopic OCT prototype system and developing the software.

3.2 Feasibility Analysis

For the measurement of the concentration of Evans blue dye using spectroscopic OCT, the absorption spectrum of Evans blue dye is the most important factor in determining the system design. Because OCT detects backscattered light intensity as a function of depth, spectroscopic OCT allows measurement of light attenuation due to the wavelength-dependent absorption of Evans blue dye in biological tissue.

The detection of Evans blue dye using spectroscopic OCT is analogous to the spectrophotometric method, which is a conventional method used for measuring the dye concentration in a homogeneous solution, except that spectroscopic OCT uses backscattered light instead of transmitted light, thereby allowing *in vivo* measurement. As in the spectrophotometric method, spectroscopic OCT requires two different wavelengths, ideally one at the absorption maximum and the other at the absorption minimum. The concentration of the dye can then be measured *in vivo* with spectroscopic OCT by applying the Beer-Lambert law to the backscattered light intensities from different layers of tissue.

It has been shown that the light absorbing characteristics of Evans blue dye in a saline solution show a distinct absorption peak over a wavelength band of ~ 150 nm centered at 610 nm [1]. For example, at 610 nm, the absorbance A is about 2.8 for a 1 cm long cell containing the dye solution at a concentration of ~0.005 %. At 750 nm, absorption is minimal and $A \sim 0$ at the same concentration. Assuming that the absorbance of water, whose $A \sim 0.18$ at 610 nm, can be neglected, the absorption coefficient for the Evans blue dye solution at a concentration of ~0.005 % can be calculated as 6.45 cm^{-1}. However, as will be discussed later in the chapter, the light source used for the spectroscopic OCT system is centered at ~650 nm instead. At this wavelength, $A \sim 2.2$ and the absorption coefficient for the same solution can be calculated as 5.07 cm^{-1}.

In OCT, the signal extinction in tissue due to scattering and absorption obeys the Beer-Lambert law. Therefore, the attenuated signal intensity I at a certain depth is given by:

$$I(L) = I_0 \exp\left[-x(L) - 2C_{EB}\alpha L\right] \tag{3.2.1}$$

where C_{EB} is the Evans blue dye concentration, α is the absorption coefficient per unit concentration, and L is the axial length of the absorbing material. $x(L)$ accounts for other scattering and absorbing contributions. The factor of 2 in the exponential kernel accounts for the round trip travel of light in the OCT sample arm.

The reported amount of Evans blue dye per eye in the rat intravitreally injected with carbonic

anhydrase I (CA-I) at a dose chosen to reach a final CA-I concentration of 2 ng/μl in the vitreous is ~180 ng [2]. Assuming that the wet retinal weight of the rat is ~4 mg per eye, the expected concentration of Evans blue leakage in retinal tissue is ~0.0045 % if the dye is homogeneously distributed within the retina.

In order to estimate light absorption in retinal tissue due to Evans blue leakage, $I(L)$ at 650 nm was computed for different edema lengths L and Evans blue dye concentrations. The results are plotted in Figure 3-1. The Evans blue dye concentration ranged from 10^{-5} to 10^{-2}. Signal transmission is plotted for axial edema lengths between 20 and 200 um, which is the full retinal thickness in the rat. The expected Evans blue leakage concentration value of 0.0045 % is shown as a vertical magenta line in all plots.

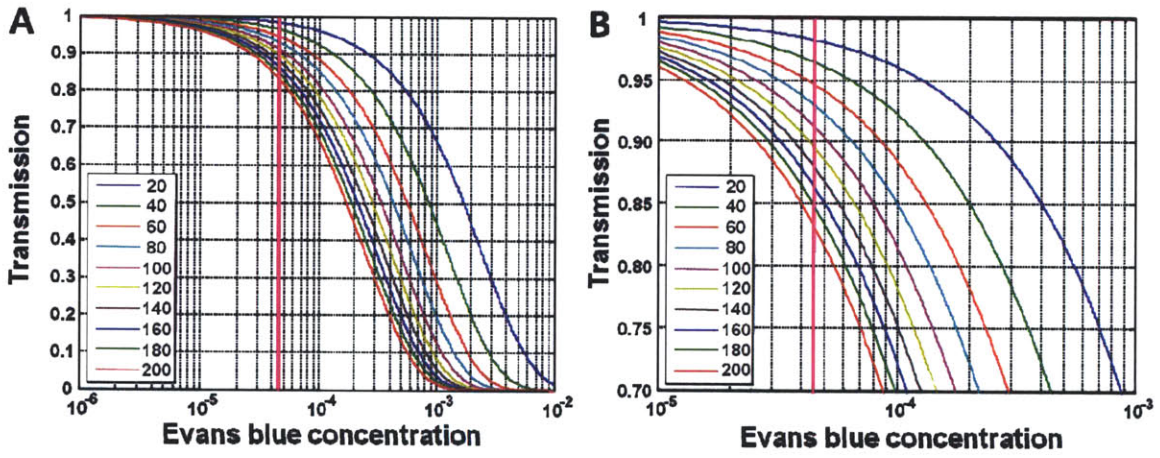

Figure 3-1. (A) Effect of Evans blue absorption in retinal tissue on transmission as a function of Evans blue dye concentration and axial edema length. (B) A close-up view of the plot in (A). The vertical lines in magenta are to indicate the expected Evans blue leakage concentration value of 0.0045 %. The unit of thickness is μm.

The transmission plots show a non-trivial effect of absorption due to Evans blue dye in the OCT signal in the given parameter ranges. At the expected retinal Evans blue dye concentration due to leakage, C_{EB} = 0.0045 %, the OCT signal gets attenuated by 17 % when a full retinal thickness

edema of L = 200 μm is assumed. However, if leakage was restricted to a smaller part of the total retina, possibly a higher Evans blue concentration could be observed in those confined leakage volumes. Hence, the OCT signal at 650 nm would be attenuated more. For instance, assuming that the Evans blue concentration were two times higher in these volumes, C_{EB} = 0.009 %, and signal damping between ~4% and ~30 % might be observed for edema lengths between 20 μm and 200 μm.

The calculations above were made using only the absorption coefficient value of Evans blue dye at 650 nm. In order to account for signal extinction due to other factors, such as scattering or absorbing structures other than the albumin-dye complex, signal variation at different depths due to focusing or sensitivity roll-off, and etc., the signal needs to be referenced to the Evans blue dye absorption minimum at 750 nm. Note that potential Evans blue leakage in the vitreous can affect the OCT signal as well. However, OCT signals in the retina can be referenced to those at the anterior surface of the retina to account for this effect.

3.3 System Overview

Figure 3-2 shows a schematic of the dual-wavelength spectroscopic OCT system. To enable simultaneous acquisition of OCT images at two different center wavelengths, a wavelength division multiplexer was used in the light source arm to combine light from two different light sources. Resulting dual bandwidth low coherence light is split equally into the sample and reference arms by a beam splitter. In the reference arm, a dispersion compensation glass block is used to match the amount of dispersion in the sample arm optics approximately. Any residual dispersion mismatch can be compensated numerically. Because light with orthogonal polarizations do not interfere with each other, the polarization controllers are used to align the polarizations of the electromagnetic fields for the maximum interference visibility. A second wavelength division multiplexer is used in the detector arm to separate the two wavelength bands before they reach the spectrometers, each of which intended for one of the wavelength bands. Figure 3-3 shows photographs of the dual-wavelength spectroscopic OCT system.

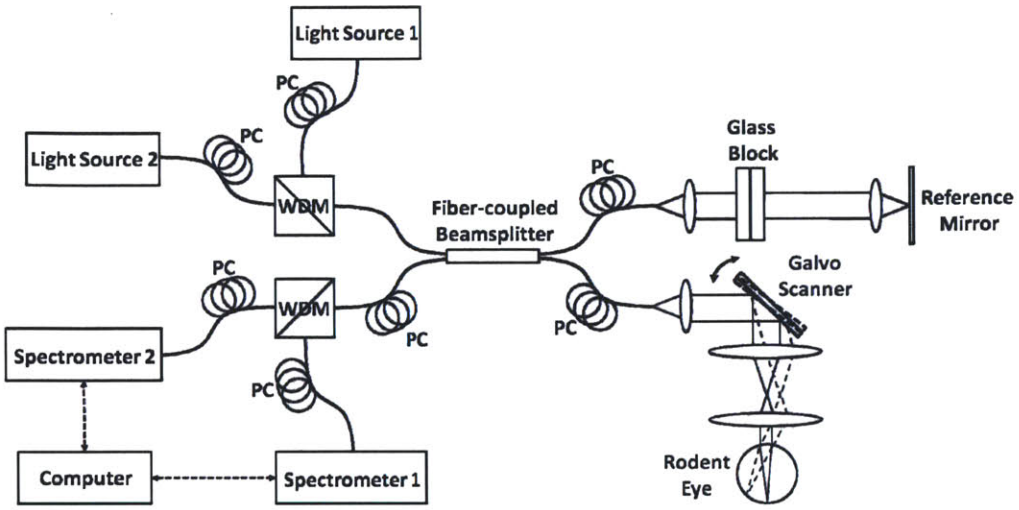

Figure 3-2. Schematic of the dual-wavelength spectroscopic OCT system. Wavelength division multiplexers are used for the source and spectrometer arms of the system to combine and separate light with two different center wavelengths. PC: polarization controller, WDM: wavelength division multiplexer.

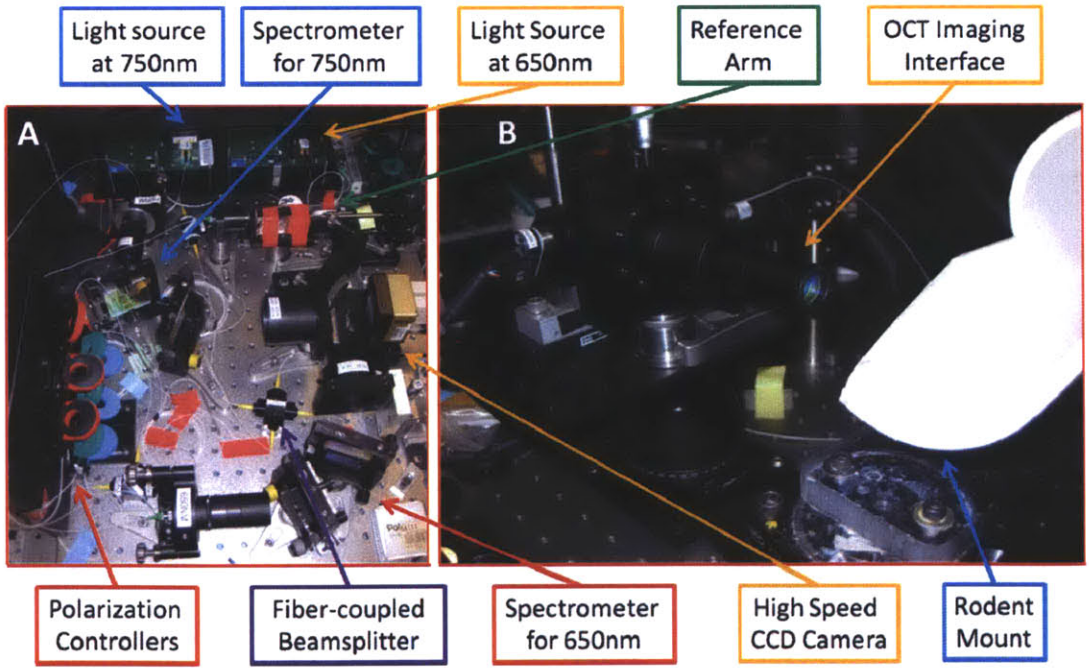

Figure 3-3. Photographs of (A) the dual-wavelength spectroscopic OCT system and (B) the OCT imaging interface and rodent mount.

3.4 Light Sources

OCT requires a temporally low-coherent light source with a broadband spectrum. Because Evans blue dye has an absorption maximum at 610 nm and a minimum at 750 nm or higher, a light source that can span both 610 nm and 750 nm simultaneously is required for the dual-wavelength spectroscopic OCT system. One type of light source that can be used for the dual-wavelength spectroscopic OCT system is a supercontinuum light source, which produces an extremely broadband spectrum by non-linear effect in a specially designed photonic crystal fiber. A typical supercontinuum light source has a spectrum that spans a wavelength range from as low as ~400 nm to over ~2000 nm. However, commercially available supercontinuum light sources are of high cost, and the short term pulse-to-pulse stability of the light source may not be good enough for quantitative spectroscopic measurement.

Therefore, as an alternative approach, the superluminescent diode (SLD) was chosen. The SLD is a good candidate for the light source for OCT because of its high short- and long-term stability and convenient turnkey operation. Because light from the SLD can be coupled into a single mode fiber to achieve spatial single mode, it is also compatible with fiber optics.

To date, the closest commercially available SLD light source to the absorption maximum of Evans blue at 610 nm in terms of the center wavelength has a full width at half maximum (FWHM) bandwidth of 12 nm centered at 650 nm. As was discussed previously, because the absorption peak of Evans blue dye is broad enough to span 650 nm, this light source can be used for the spectroscopic measurement of Evans blue dye concentration. The theoretical axial resolution achievable with this light source is ~ 11.5 μm in tissue assuming an index of refraction of $n = 1.35$ in tissue. The measured output power of the light source was 0.95 mW.

An SLD with a FWHM bandwidth of 21 nm centered at 750 nm was used as the second light source for the reference at the absorption minimum of Evans blue. The theoretical axial resolution for this light source can be calculated as 9 um in tissue. The output power of the light source was 2.3 mW. Figure 3-4 shows the spectra of the two light sources measured with the dual-wavelength spectroscopic OCT spectrometer.

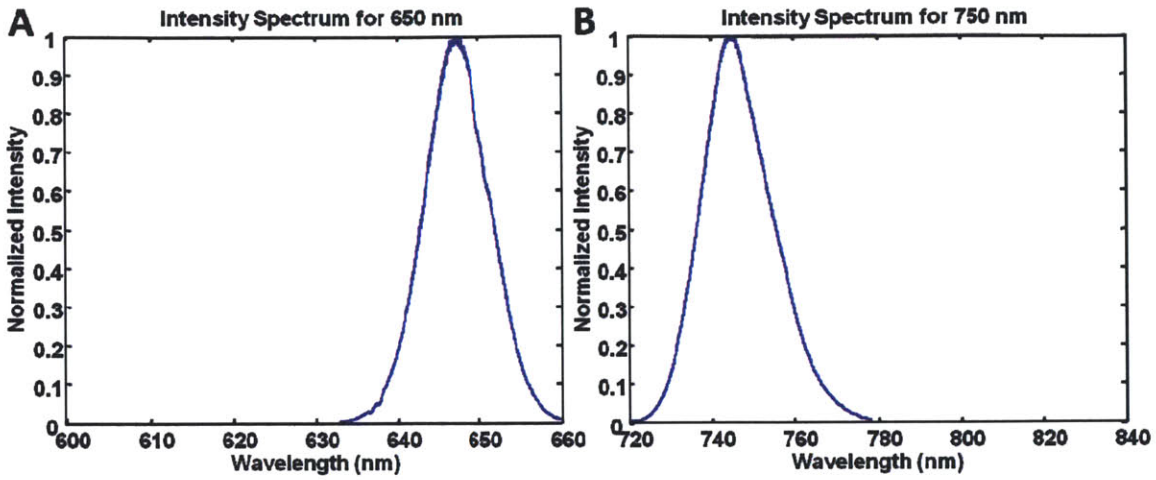

Figure 3-4. (A) The measured spectrum of the light source centered at 650 nm and (B) the measured spectrum of the light source centered at 750 nm. The nominal FWHM bandwidths of the two light sources are ~12 nm and ~21 nm, respectively.

3.5 Interferometer and WDM

Interferometer

The two light sources are combined with a wavelength-division multiplexer in the light source arm of the dual-wavelength spectroscopic OCT system. Therefore, a broadband interferometer that has a flat 50 / 50 coupling ratio over the wavelength band from ~610 nm to ~ 780 nm is required for the dual-wavelength OCT system. Although a fused fiber coupler, which does not have any bulk component, is typically desired for spectral / Fourier domain OCT due to its high efficiency, it is challenging to manufacture a fused fiber coupler with a flat coupling ratio over this wavelength range. Therefore, a fiber-coupled bulk 50 / 50 beamsplitter was used instead in the system. The advantage of the fiber-coupled bulk beamsplitter is that it has a very flat spectral coupling ratio. However, the main disadvantage of it is that it is inherently less efficient than a fused fiber coupler because light needs to be coupled into a single mode fiber from free space in the fiber-coupled bulk beamsplitter design.

Wavelength Division Multiplexer

The wavelength-division multiplexers (WDM) in the dual-wavelength spectroscopic OCT system need to be used carefully because of their polarization dependency. A typical fiber-coupled bulk optics WDM utilizes a dielectric mirror that has transmission and reflection bands. However, because the dielectric mirrors in WDMs are typically used at an incidence angle of 45°, group delay dispersions for transverse electric (TE) and transverse magnetic (TM) waves are necessarily different. This means that if the polarization of the input light is varying, different polarizations experience different amount of dispersions. Although it is possible to compensate for a known amount of group delay dispersion physically or numerically if there is no polarization dependency, the polarization-dependent group delay dispersion induced by the WDM is very difficult to compensate for.

The polarization dependent group delay dispersion can be considered as a wavelength-dependent wave plate, which delays the phases of different polarizations by different amounts. Just as a typical wave plate changes the polarization of input light, the WDM can also change the polarization of input light. However, because the group delay dispersion is wavelength-dependent, the polarization of output light is also wavelength-dependent. This can become a major problem for the OCT spectrometer because the diffraction grating used in the spectrometer has a polarization-dependent efficiency. This means that the shape of the interference spectrum will be distorted by the polarization-dependent efficiency of the diffraction grating if the WDMs are not used carefully.

One way to overcome this problem is to align the input polarization purely to either the TE or TM polarization of the WDM to avoid the polarization-dependency in the group delay dispersion. As long as the group delay dispersion is not polarization-dependent, it can be compensated numerically. To have a full control over the polarization state in the OCT system at all necessary intermediate locations, several polarization controllers are used as shown in Figure 3-2.

There are several requirements for the polarization state of light in the dual-wavelength spectroscopic OCT system. First, because the rodent eye can be birefringent, the input

polarization at 650 nm and 750 nm at the sample arm should be identical to experience the same amount of polarization artifact at the two wavelength bands. Second, the input polarization state at the first WDM should be either purely TE or purely TM. Third, the reference arm polarization state should be matched to the sample arm polarization state to maximize the interference spectrum visibility. Fourth, the input polarization state at the second WDM should be purely TE or TM as well. Lastly, the input polarization to the spectrometer should be adjusted to maximize the efficiency of the diffraction grating. Figure 3-5 shows the detected spectra at 650 nm when the polarization state is carefully adjusted and when it is not adjusted.

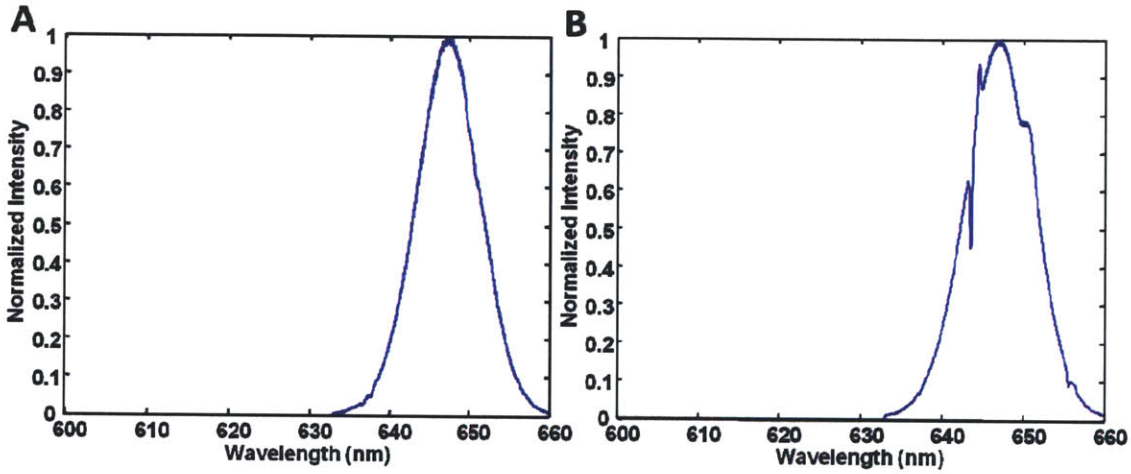

Figure 3-5. The effect of the polarization state on the shape of the reference spectrum. (A) The detected spectrum at 650 nm when the polarization state is carefully adjusted. (B) The detected spectrum at 650 nm when the polarization state is not adjusted.

3.6 Reference Arm

Because the output power of the light source centered at 650 nm and that centered at 750 nm were different, the back-coupled power levels from the reference arm at the two center wavelengths need to be adjusted independently to avoid spectrometer saturation. Although a neutral density filter with an adjustable optical density value is typically used in the OCT reference arm, it is not possible to adjust the power level at two different wavelength bands independently with a neutral density filter. Therefore, in the reference arm of the dual-wavelength spectroscopic OCT system, chromatic aberration of the lens in front of the reference

arm mirror is utilized. Due to chromatic aberration, different wavelength components have slightly different focal lengths. A singlet lens was used instead of an achromat in front of the reference mirror to maximize chromatic aberration. By adjusting the reference mirror position with respect to the singlet lens carefully, the reference power levels at 650 nm and 750 nm could be adjusted independently.

3.7 OCT Imaging Interface

Most OCT patient interfaces developed for imaging the human retina have the pivot of scanning located at the pupil of the eye. The advantages of this configuration are that a large maximum scan area is achieved without vignetting and that it does not require a special contact lens or cover glass in front of the eye. The ability to scan a large area without vignetting is expected to help in generating large two- and three-dimensional vascular permeability maps. Moreover, since contact lenses or cover glasses in front of the eye may alter intraocular pressure, the ability to scan without an additional optical element in front of the eye may be very important as it precludes many sources of measurement variability. An adjustable focus is helpful because rat eyes are expected to be slightly different from one another.

For the dual-wavelength spectroscopic OCT system, a diffraction-limited small animal imaging interface with an adjustable focus and the pivot of scanning located at the pupil of the rodent eye was developed. Figure 3-6 shows a schematic of the OCT imaging interface. In the OCT imaging interface, light from the optical fiber is collimated with a collimating lens. The collimated beam is then scanned by a galvanometer-actuated scanning mirror pairs that scan the beam in the transverse directions on the rodent retina. The distance between the scan lens and the objective lens complex is adjustable for focus adjustment to account for variations in individual rat eyes. The maximum scan angle used in the OCT imaging interface is ±5°. The corresponding scan range on the retina is ±1 mm. Compared to the scan range of the telecentric scanning imaging interface, which is another commonly used imaging interface configuration for rodent retinal imaging, the scan range of ±1 mm of this pivoted configuration is ~60 % larger. In the telecentric interface, the cornea needs to be flattened by a cover glass, and the field of view is limited by the dilated pupil diameter.

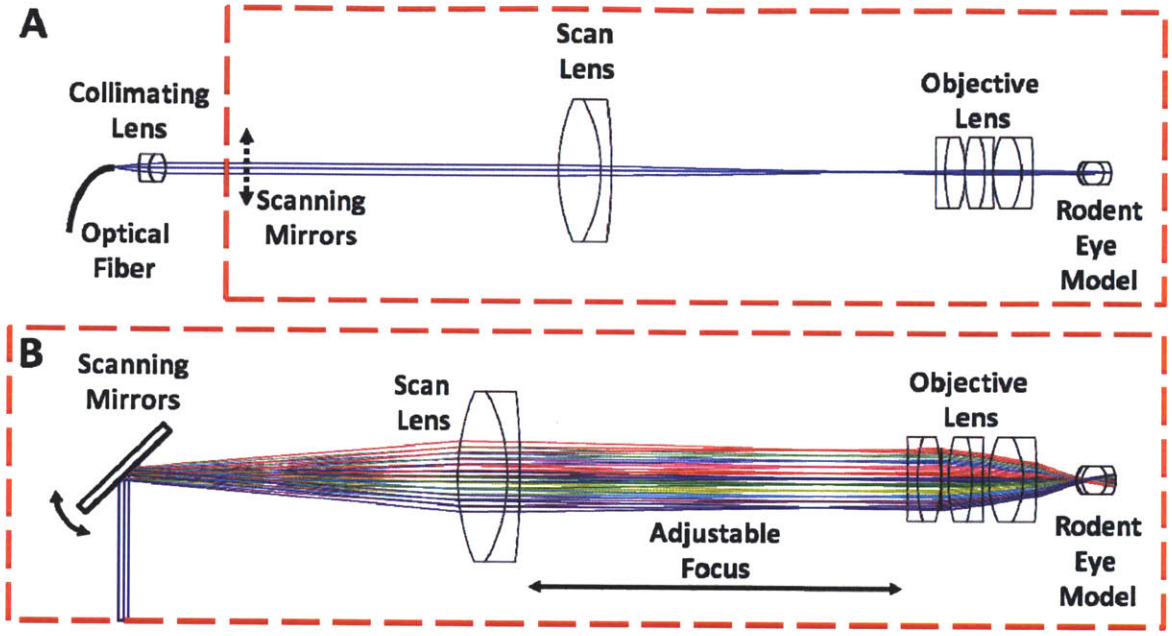

Figure 3-6. (A) Schematic of the OCT imaging interface for the dual-wavelength spectroscopic OCT system. (B) Close-up view of the imaging interface in (A) with multiple scan angles. The distance between the scan lens and the objective lens complex is adjustable for focus adjustment.

A rat eye model was used in the ray tracing software ZEMAX in designing the imaging interface of the dual-wavelength spectroscopic OCT system [3]. A diffraction-limited performance was achieved at 650 nm and 750 nm simultaneously over the entire scan range except near the ends of the range of the imaging interface. Figure 3-7 summarizes diffraction-limited performance of the imaging interface. The spot diagram shows that the imaging interface achieves the diffraction-limited spot size at 650 nm and 750 nm simultaneously for all scan angles except near the ends of the imaging range. The modulation transfer function also supports diffraction-limited performance. The diffraction-limited spot size on the retina is simulated to be ~13 μm. The output power measured at the cornea at 650 nm was 270 μW and that at 750 nm was 600 μW. The measured power transmission of the imaging interface was 85 % single pass.

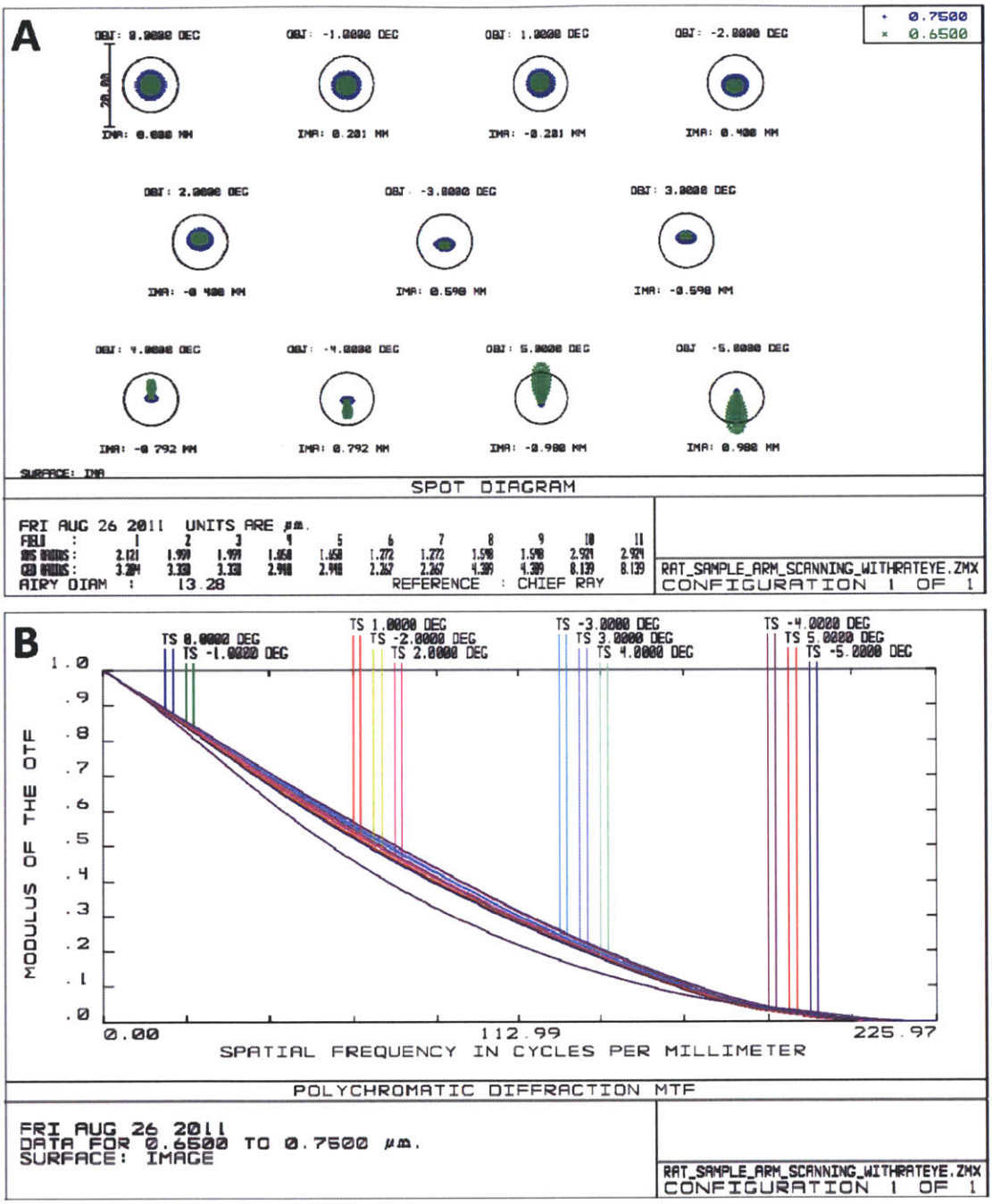

Figure 3-7. Diffraction-limited performance of the OCT imaging interface for the dual-wavelength spectroscopic OCT system. (A) The spot diagram and (B) the modulated transfer function simulated by ZEMAX.

3.8 Spectrometer

Figure 3-8 shows a schematic of the dual-wavelength spectroscopic OCT spectrometer. Because the bandwidths of the two light sources used in the spectroscopic system are not very broad compared to that of an ultrahigh resolution OCT system, the spectroscopic OCT spectrometer does not require a large number of pixels to achieve an imaging range necessary for small animal imaging. Therefore, instead of using two cameras, a single CCD camera is shared by the 650 nm and 750 nm wavelength bands to avoid synchronization problems. In order to achieve good sensitivity roll-off performance and imaging range, two diffraction gratings were used to maximize spectral dispersion although using two gratings made the spectrometer less efficient. The 650 nm beam was re-directed to the CCD camera by folding the beam with a fold mirror. By adjusting the fold mirror and focusing lens for the beam centered at 650 nm carefully, the two wavelength bands can be aligned with respect to the CCD camera independently.

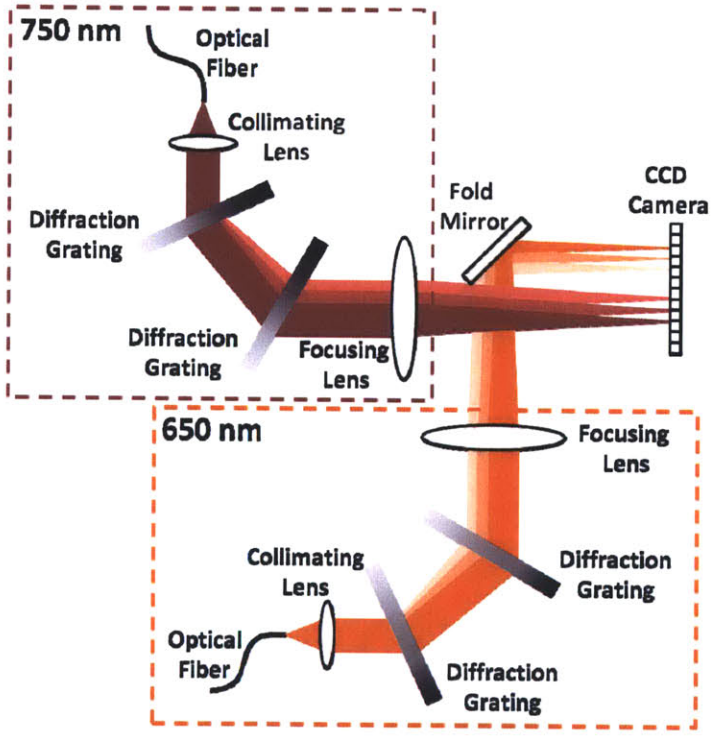

Figure 3-8. Schematic of the dual-wavelength spectroscopic OCT spectrometer. Both the 650 nm spectrum and 750 nm spectrum are acquired by a single CCD camera. The 650 nm beam is folded by 90° with a fold mirror to direct the beam to the CCD camera.

Optics in the spectrometer was chosen carefully using ZEMAX simulation to achieve diffraction-limited performance at both 650 nm and 750 nm over the entire bandwidths to maximize system sensitivity. Figure 3-9 summarizes diffraction-limited performance of the imaging interface. The spot diagrams show that the spectrometer achieves the diffraction-limited spot size smaller than the camera pixel size, which is 28 μm, at all wavelengths spanned by the light sources.

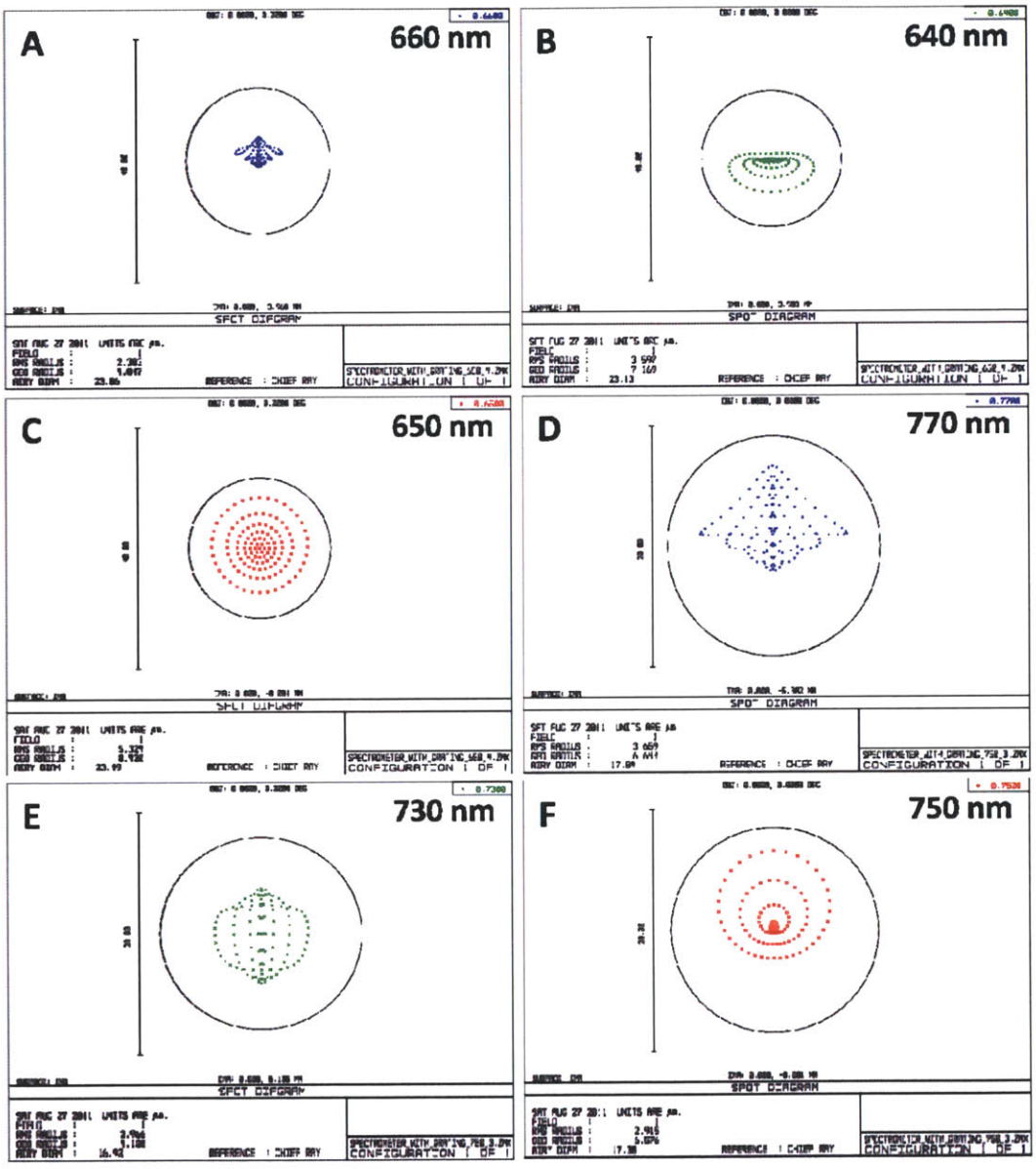

Figure 3-9. Diffraction-limited performance of the spectrometer for the dual-wavelength spectroscopic OCT system. The spot diagrams show diffraction-limited performance at all wavelengths spanned by the light sources.

3.9 Image Acquisition and Signal Processing

Custom-built LabVIEW software was used to control image acquisition. A personal computer equipped with a high-speed analog output board and a camera frame grabber was used to trigger the CCD camera for image acquisition, send the scan trajectory to the galvanometer controller cards, and to transport frames captured by the camera to computer memory. The LabVIEW software was capable of displaying a real-time preview of the OCT cross-sections at 650 nm and 750 nm simultaneously. For the ease of alignment, a real-time *en face* projection preview was also implemented in the LabVIEW software. The LabVIEW software was built on an earlier version of the acquisition software written by Jonathan Liu and other members of our group. Signal processing and image analysis was performed in MATLAB.

Signal processing steps used for the data acquired with the dual-wavelength spectroscopic OCT system are in general similar to what was described in Chapter 2. However, the only major difference is that there are two wavelength bands simultaneously acquired by a single CCD camera in the spectrometer. In dual-wavelength spectroscopic OCT signal processing, two different wavelength bands are used and interference spectra from each of the bands is Fourier transformed independently to obtain simultaneously acquired image pairs, one at 650 nm and the other at 750 nm. Therefore, it is necessary to recalibrate the interference spectrum carefully so that the images acquired simultaneously at 650 nm and 750 nm retain the same axial scale.

For recalibration purposes, the interference spectrum with a single reflector in the sample arm was acquired at two different delays using both of the light sources simultaneously. As in Chapter 2, two different delays were used to cancel out the residual dispersion mismatch. The interference spectra at the two wavelength bands need to be acquired simultaneously because a given optical path length difference needs to appear at the same depth in the Fourier domain OCT images. At the same time, the total number of pixels per axial scan in the Fourier domain should be the same for the images acquired at 650 nm and 750 nm.

First, the interference spectrum centered at 650 nm was recalibrated using the method described in Chapter 2. As in Chapter 2, the total range of the unwrapped phase of the interference

spectrum divided by the number of pixels desired provides the phase increment between neighboring pixels, which determines the frequency. The same phase increment was used for recalibrating the interference spectrum centered at 750 nm. The interference spectra at 650 nm and 750 nm were padded with zeros to ensure that the resultant numbers of samples per axial scan were identical for the two wavelengths. Because the phase increment between neighboring samples for the interference spectrum for a single reflector and the total number of samples per axial scan are the same for the two wavelengths after zero-padding, the resultant interpolation locations determined by this method ensures that the OCT images acquired at 650 nm and 750 nm have the same axial scale. This is graphically illustrated in Figure 3-10.

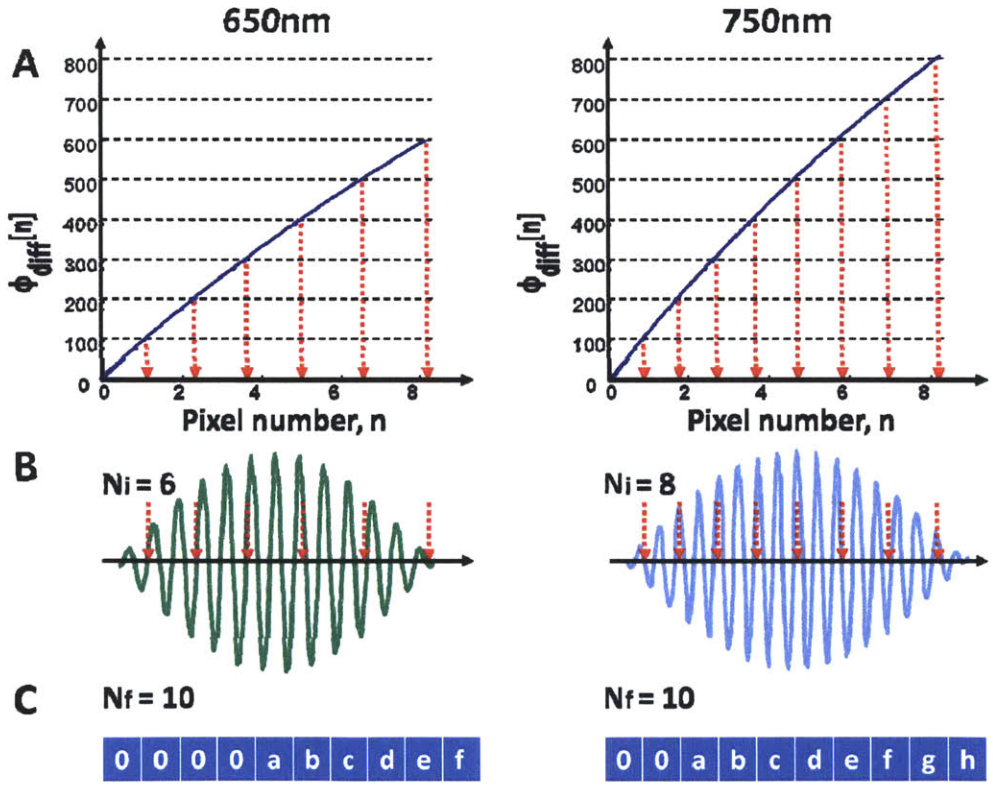

Figure 3-10. Recalibration of the dual-wavelength OCT interference spectrum. (A) The same phase increment is chosen for both 650 nm and 750 nm. (B) The interference spectra are resampled accordingly. (C) The final sequences of discrete samples are padded with zeros so that the total number of samples per axial scan is the same for 650 nm and 750 nm. a, b, c … : arbitrary sample values.

3.10 System Performance

The sensitivity of the system calculated using the convention described in Chapter 2 was 100 dB at 650 nm and 102.3 dB at 750 nm. The camera speed used for sensitivity measurement and data acquisition in general was 25 kHz. The output power measured at the cornea was 270 μW at 650 nm and 600 μW at 750 nm. The measured nominal imaging range was 3 mm in air or 2.2 mm in tissue. Although physical aliasing occurs in the spectrum centered at 750 nm before the optical path length difference in air becomes 3 mm, the nominal imaging range of the dual-wavelength spectroscopic OCT system was still determined by the spectrum centered at 650 nm because the phase increment value used for spectrum recalibration was calculated with the spectrum centered at 650 nm. The full-width at half-maximum axial resolution of the system in tissue was ~12.1 μm at 650 nm and ~8.7 μm at 750 nm. The spectrometer roll-off as a function of depth is shown in Figure 3-11. The magnitude of the Fourier transform of the interference spectrum is plotted.

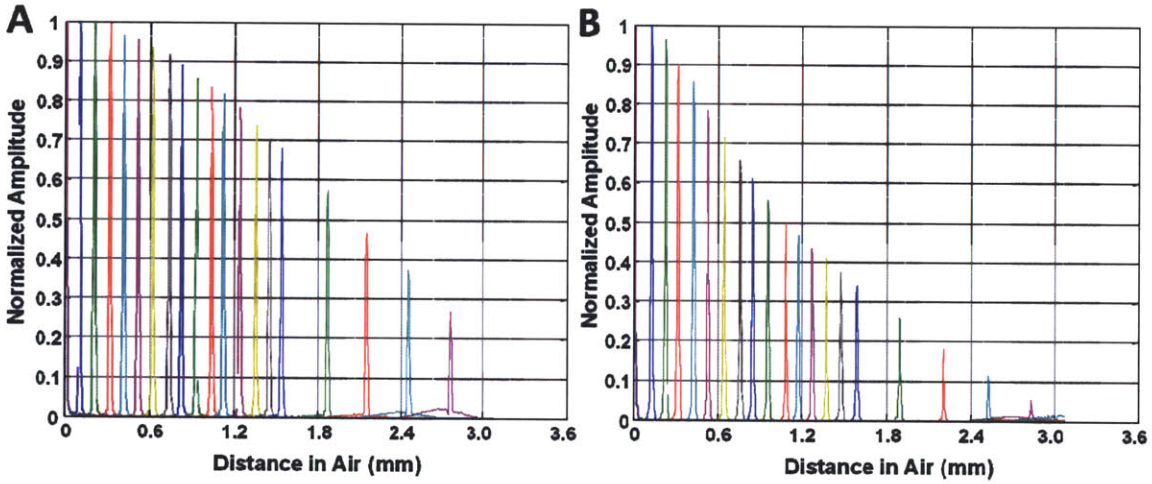

Figure 3-11. Spectrometer roll-off in the dual-wavelength spectroscopic OCT system. (A) Spectrometer roll-off at 650 nm in the linear amplitude scale. (B) Spectrometer roll-off at 750 nm in the linear amplitude scale.

References

1. E. D. F. Costa, E. B. Rodrigues, M. E. Farah, E. Dib, F. Penha, O. Magalhaes, B. A. Furlani, A. A. S. Lima, A. de Miranda, and M. Maia, "Vital Dyes and Light Sources for Chromovitrectomy: Comparative Assessment of Osmolarity, pH, and Spectrophotometry," Invest. Ophthalmol. Vis. Sci. **50**, 385-391 (2009).

2. B. B. Gao, A. Clermont, S. Rook, S. J. Fonda, V. J. Srinivasan, M. Wojtkowski, J. G. Fujimoto, R. L. Avery, P. G. Arrigg, S. E. Bursell, L. P. Aiello, and E. P. Feener, "Extracellular carbonic anhydrase mediates hemorrhagic retinal and cerebral vascular permeability through prekallikrein activation," Nat. Med. **13**, 181-188 (2007).
3. A. Chaudhuri, P. E. Hallett, and J. A. Parker, "Aspheric curvatures, refractive-indexes and chromatic aberration for the rat eye," Vision Res. **23**, 1351-1363 (1983).

Chapter 4

Spectroscopic OCT Imaging and Data Analysis

4.1 Overview

Enabling *in situ* measurement of changes in vascular permeability without the need to remove or process specimens, spectroscopic OCT using Evans blue dye as an absorbing contrast agent is expected to overcome many of the limitations of conventional methods used for measuring vascular permeability changes in small animal models. For this study, the dual-wavelength spectroscopic OCT system discussed in Chapter 3 was used for *in vivo* measurement of changes in vascular permeability in the rat retina. The purpose of this chapter is to discuss spectroscopic OCT imaging and data analysis for measuring retinal vascular permeability changes in small animal models. The spectroscopic OCT system, animal procedures, and scan protocols used in this study are summarized. Data processing methods for spectroscopic analysis are discussed, and preliminary results demonstrating wavelength-dependency of the OCT signal in the presence of Evans blue dye are shown. Dr. Bernhard Baumann from our group collaborated in this study and provided significant amount of input in determining the direction of the study.

4.2 Background

Evans blue dye is a standard intravascular dye used for nonradioactive quantitation of blood-retinal barrier breakdown in small animal models [1-3]. Evans blue dye has an important property that it binds to the blood plasma protein albumin irreversibly when injected into the bloodstream of small animals. Because of this property, whenever blood plasma extravasates from blood vessels, the albumin-dye complex exudes into surrounding tissue as well [4]. Moreover, the clearance time of Evans blue dye in the bloodstream of small animals is significantly longer than those of other commonly used dyes such as indocyanine green and fluorescein, thereby making Evans blue suitable for long time progression studies. Evans blue

absorption in saline solution has a maximum at ~610 nm, while absorption at 750 nm is negligible [5], and it is possible to measure Evans blue concentration with optical methods. Therefore, it is desirable to develop a spectroscopic OCT technique that uses Evans blue dye as an absorbing contrast agent to measure vascular permeability changes in small animal models.

Previous work has shown that intravitreal injection of carbonic anhydrase I (CA-I) in rats alters retinal pH regulation leading to changes in retinal vascular permeability [6]. In this study, an animal model with increased retinal vascular permeability was generated by intravitreal injection of carbonic anhydrase I.

4.3 Methods

Spectroscopic OCT System

Figure 4-1 shows the dual-wavelength spectroscopic OCT system used in this study to measure Evans blue concentration *in vivo*. The system is described in detail in Chapter 3.

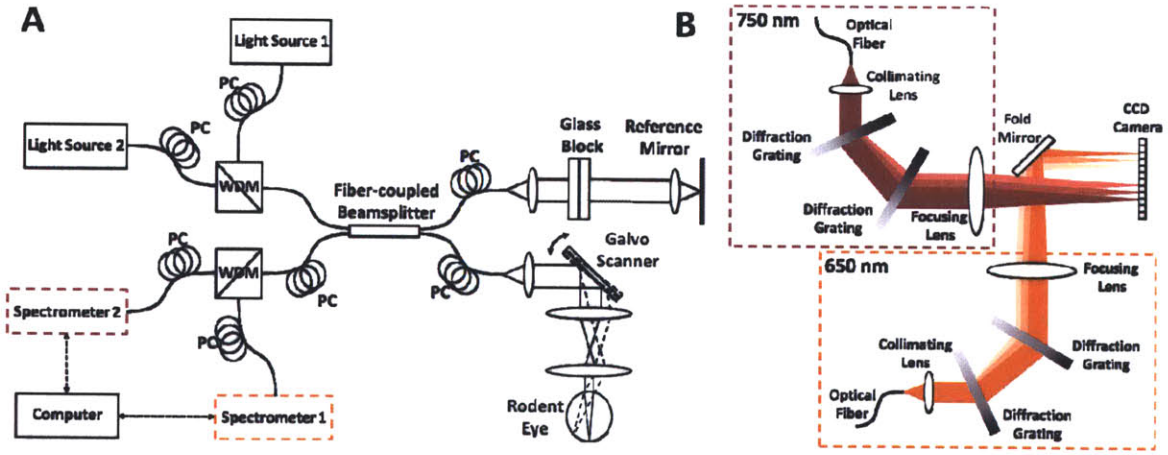

Figure 4-1. (A) Schematic of the dual-wavelength spectroscopic OCT system. Light sources 1 and 2 are centered at 650 nm and 750 nm, respectively. PC: polarization controller, WDM: wavelength division multiplexer. (B) Schematic of the dual-wavelength spectroscopic OCT spectrometer.

Animal Procedures

A normal male Sprague-Dawley rat was anesthetized with ketamine / xylazine (ketamine 40-80 mg/kg IP, xylazine 5-10 mg/kg IP). After anesthesia, the eyes were dilated with tropicanimide (Mydriacyl, 1%) applied topically. For the ease of Evans blue dye injection, a catheter was inserted into the tail vein. Before intravitreal injection, baseline OCT imaging was performed with the dual-wavelength spectroscopic OCT system. After baseline imaging, intravitreal injection of CA-I solution prepared in saline was performed on the right eye to reach a physiologically relevant concentration of 2 ng/μl. The contralateral eye was injected with saline only as control to see if there is any difference in retinal vascular permeability between the two eyes [6]. The total of 5 μl of the active agent solution or saline alone was injected into the vitreous. 15 minutes after intravitreal injection, the rat was imaged with the spectroscopic OCT system before Evans blue injection. Immediately after spectroscopic OCT imaging, Evans blue dye was injected via the catheter inserted into the tail vein at a dose of 45 mg/kg. Spectroscopic OCT imaging was performed 0, 1, and 2 hours after the tail vein injection of Evans blue dye. Upon completion of imaging, the animal was sacrificed with CO_2. All animal procedures were performed under an approved protocol by the Committee on Animal Care (CAC) at MIT.

Scan Protocol and Data Analysis

An OCT scan pattern of 500 by 500 samples over an area of 1.2 mm by 1.2 mm on the retina was used for spectroscopic OCT imaging. The isotropic scan pattern was chosen for better visualization of spectroscopic data with the *en face* projection view. The scan pattern was centered at the optic disc for all OCT scans. At an imaging speed of 25,000 axial scans per second, it took ~12 seconds to acquire one volumetric scan, including the galvanometer scanner flyback time. All the OCT images were acquired with the posterior part of the eye located closer to the zero delay compared to the anterior part of the eye to counter the signal attenuation in depth within tissue with the spectrometer roll-off. Multiple data analysis steps, including spectrometer roll-off correction, image averaging for speckle reduction, as well as the routine OCT signal processing procedure, have been implemented using MATLAB for accurate visualization of spectroscopic data.

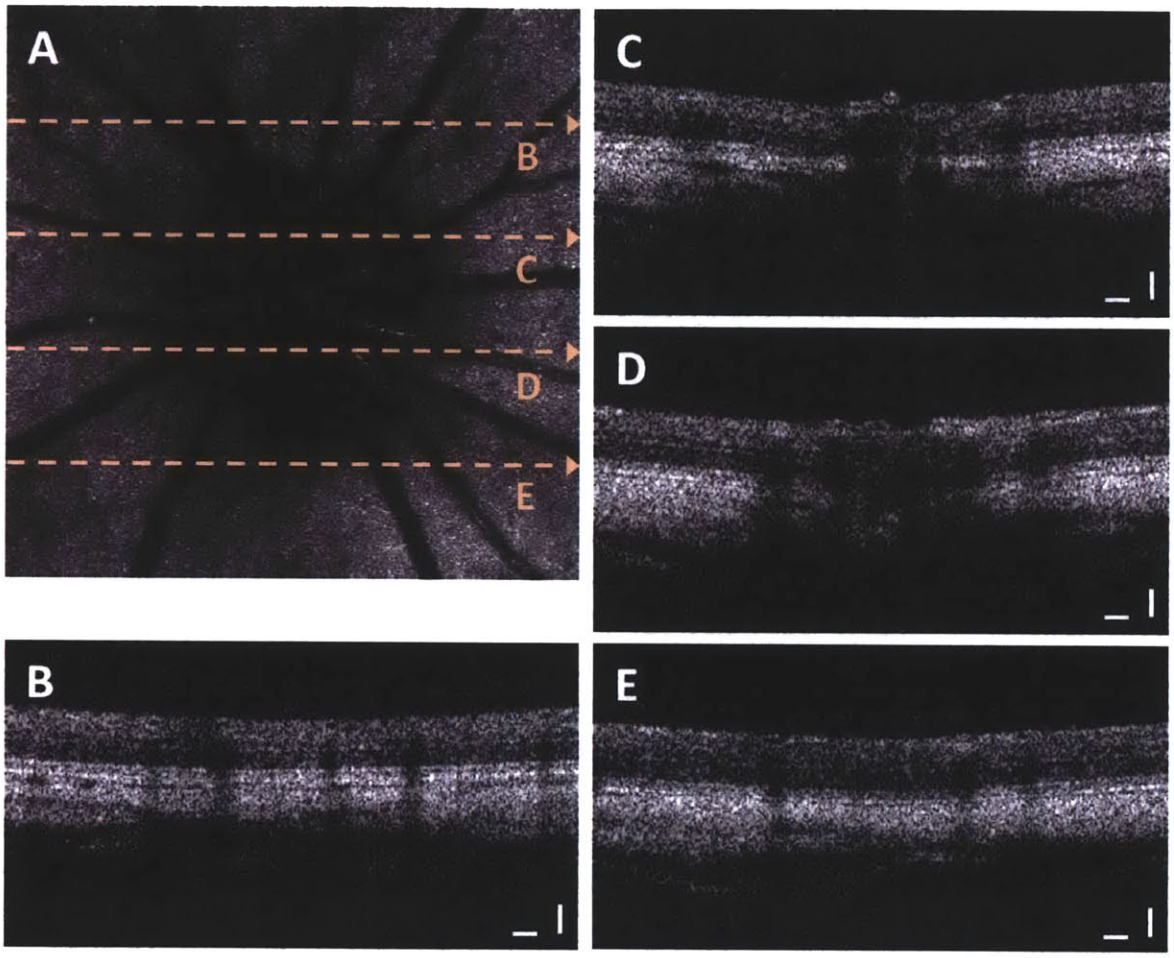

Figure 4-2. Retinal OCT images of a normal Sprague-Dawley rat acquired by the 650 nm channel of the dual-wavelength spectroscopic OCT system. (A) An OCT *en face* projection image created from a volumetric data set of 500 by 500 axial scans over an area of 1.2 mm by 1.2 mm centered at the optic nerve head. (B-E) Examples of OCT cross-sectional images from the positions of the dotted lines indicated on the OCT *en face* projection image. The cross-sectional images are displayed in the logarithmic scale. Scale bar: 100 μm.

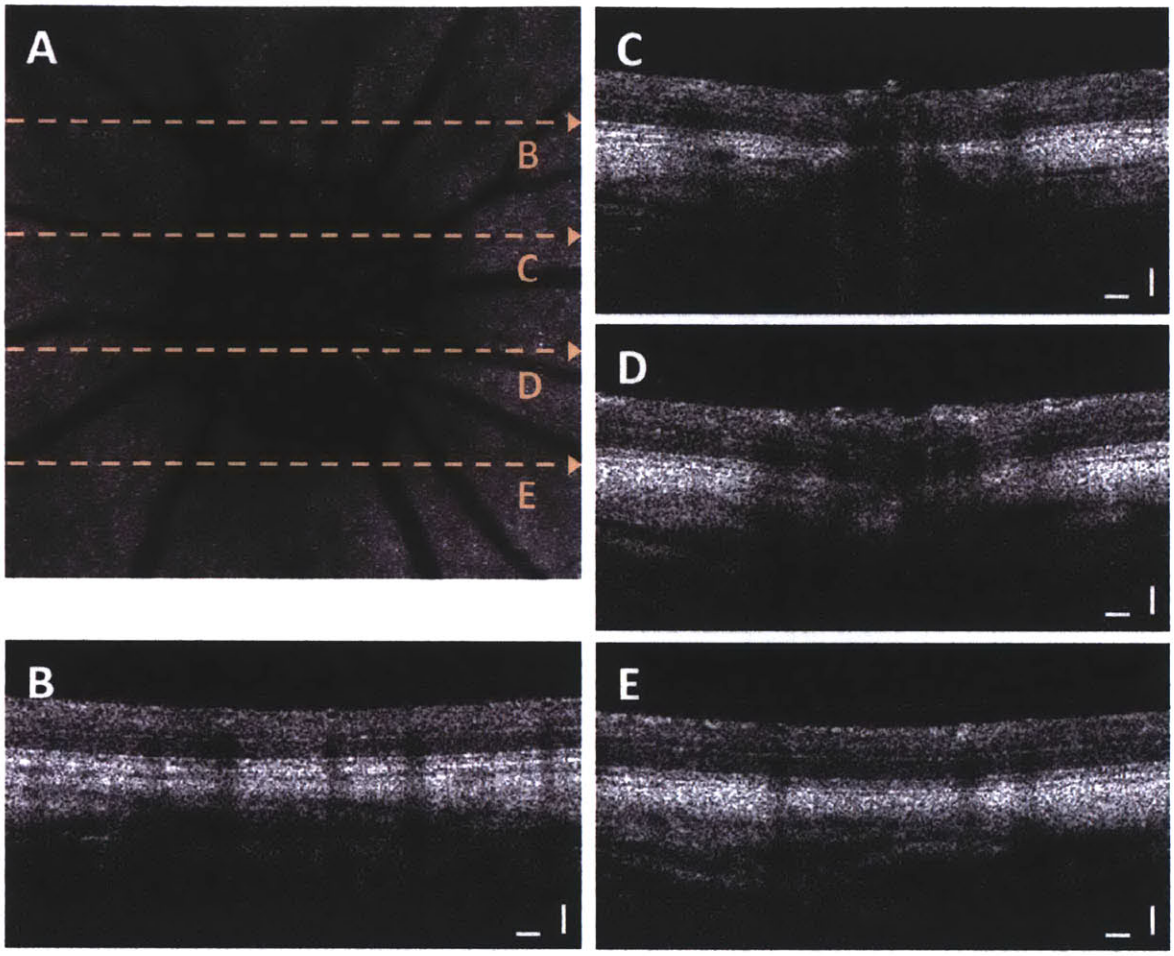

Figure 4-3. Retinal OCT images of a normal Sprague-Dawley rat acquired by the 750 nm channel of the dual-wavelength spectroscopic OCT system. (A) An OCT *en face* projection image created from a volumetric data set of 500 by 500 axial scans over an area of 1.2 mm by 1.2 mm centered at the optic nerve head. (B-E) Examples of OCT cross-sectional images from the positions of the dotted lines indicated on the OCT *en face* projection image. The cross-sectional images are displayed in the logarithmic scale. Scale bar: 100 μm.

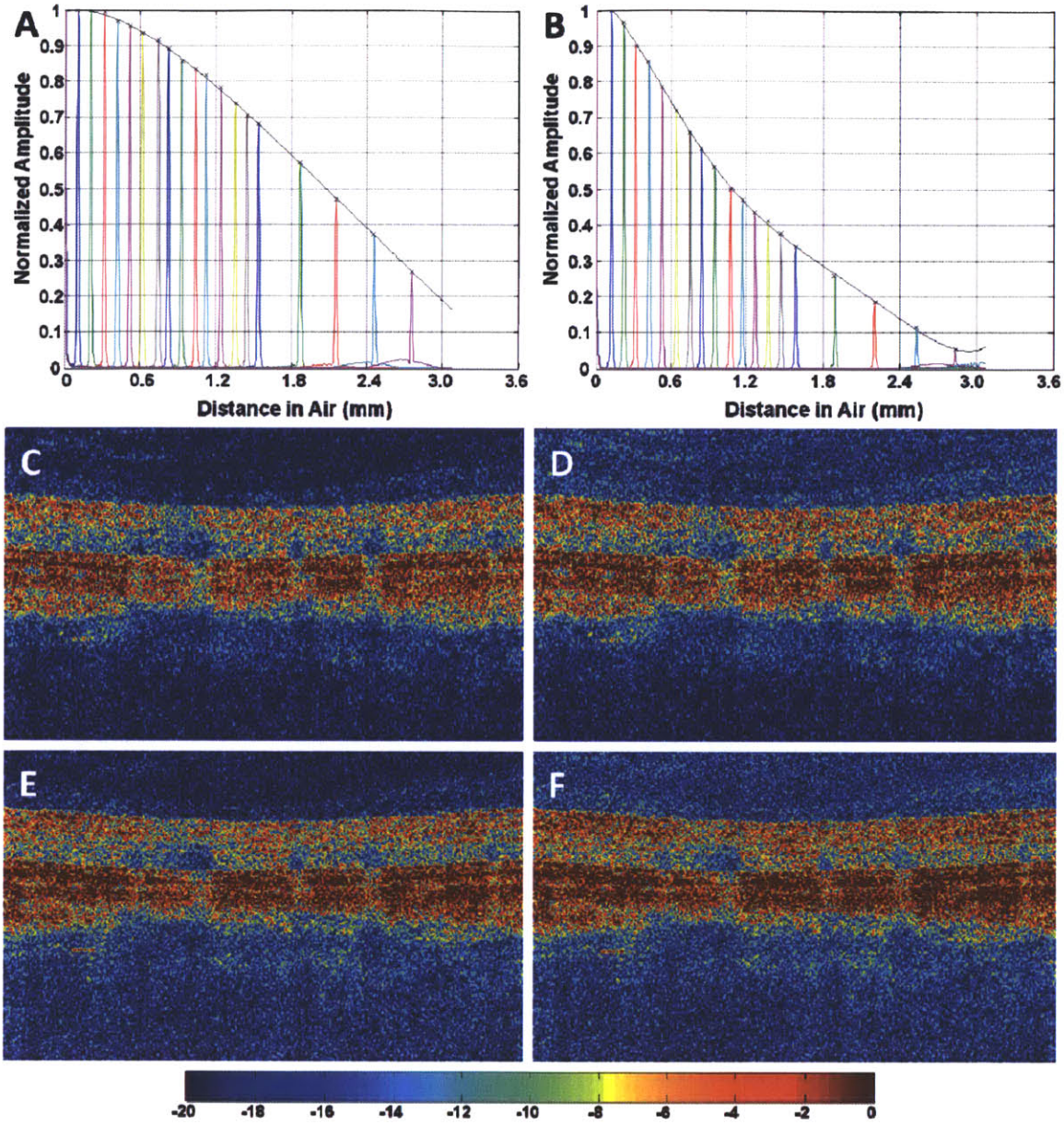

Figure 4-4. Roll-off corrected cross-sectional OCT images. (A) The spectrometer roll-off of the 650 nm channel in the linear amplitude scale. (B) The spectrometer roll-off of the 750 nm channel. (C) An OCT cross-sectional image from the 650 nm channel before roll-off correction. (D) A roll-off corrected version of the image shown in (C). (E) An OCT image from the 750 nm channel before roll-off correction. (F) A roll-off corrected version of the image shown in (E). The cross-sectional images (C-F) are displayed in the logarithmic scale.

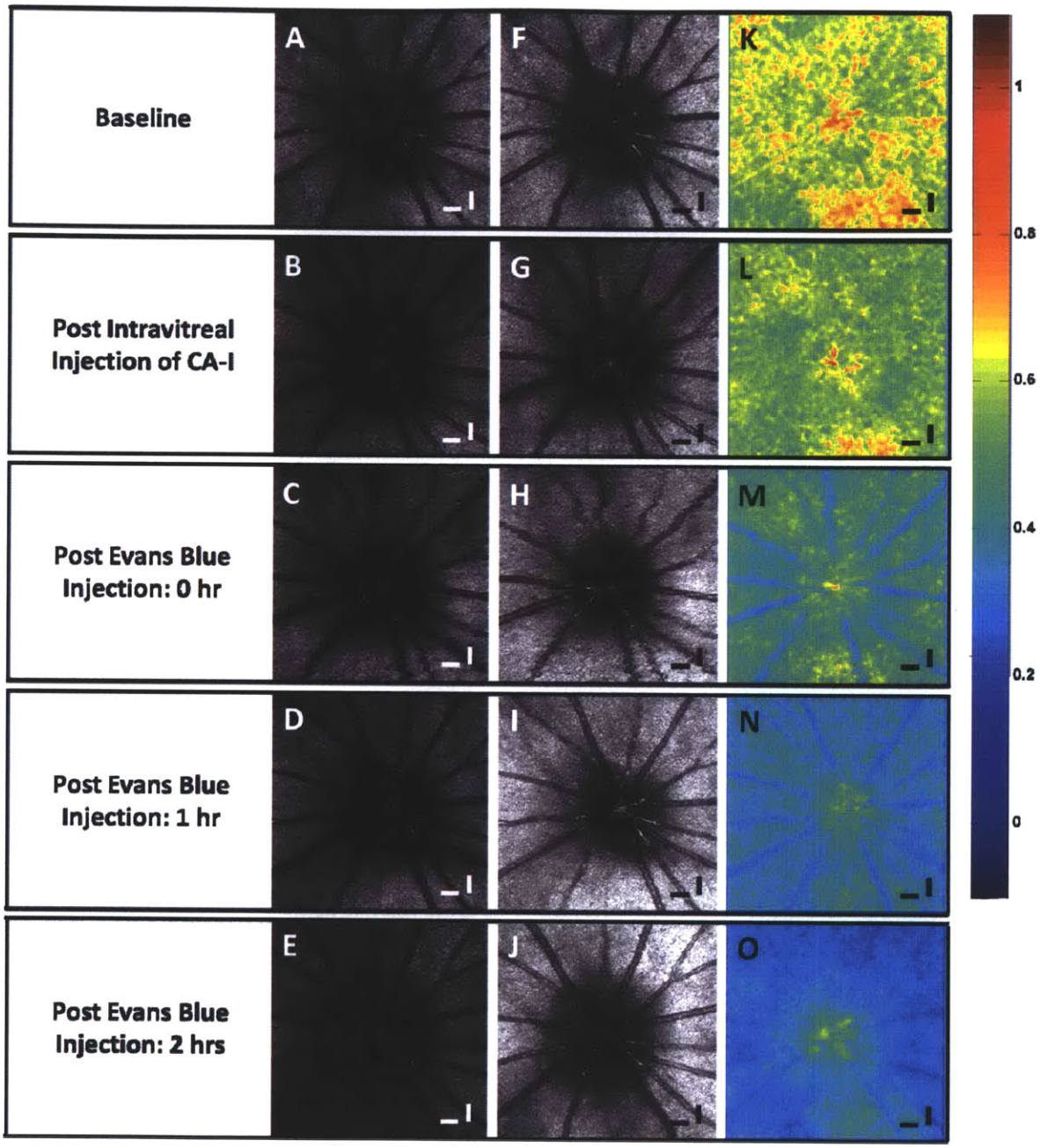

Figure 4-5. Visualization of wavelength-dependent absorption due to Evans blue dye using normalized *en face* ratio images. (A-E) OCT *en face* projection images from the 650 nm channel at multiple time points. (F-J) OCT *en face* projection images from the 750 nm channel at multiple time points. (K-O) Normalized *en face* ratio images obtained by dividing the images acquired at 650 nm with those acquired at 750 nm. Scale bar: 100 μm.

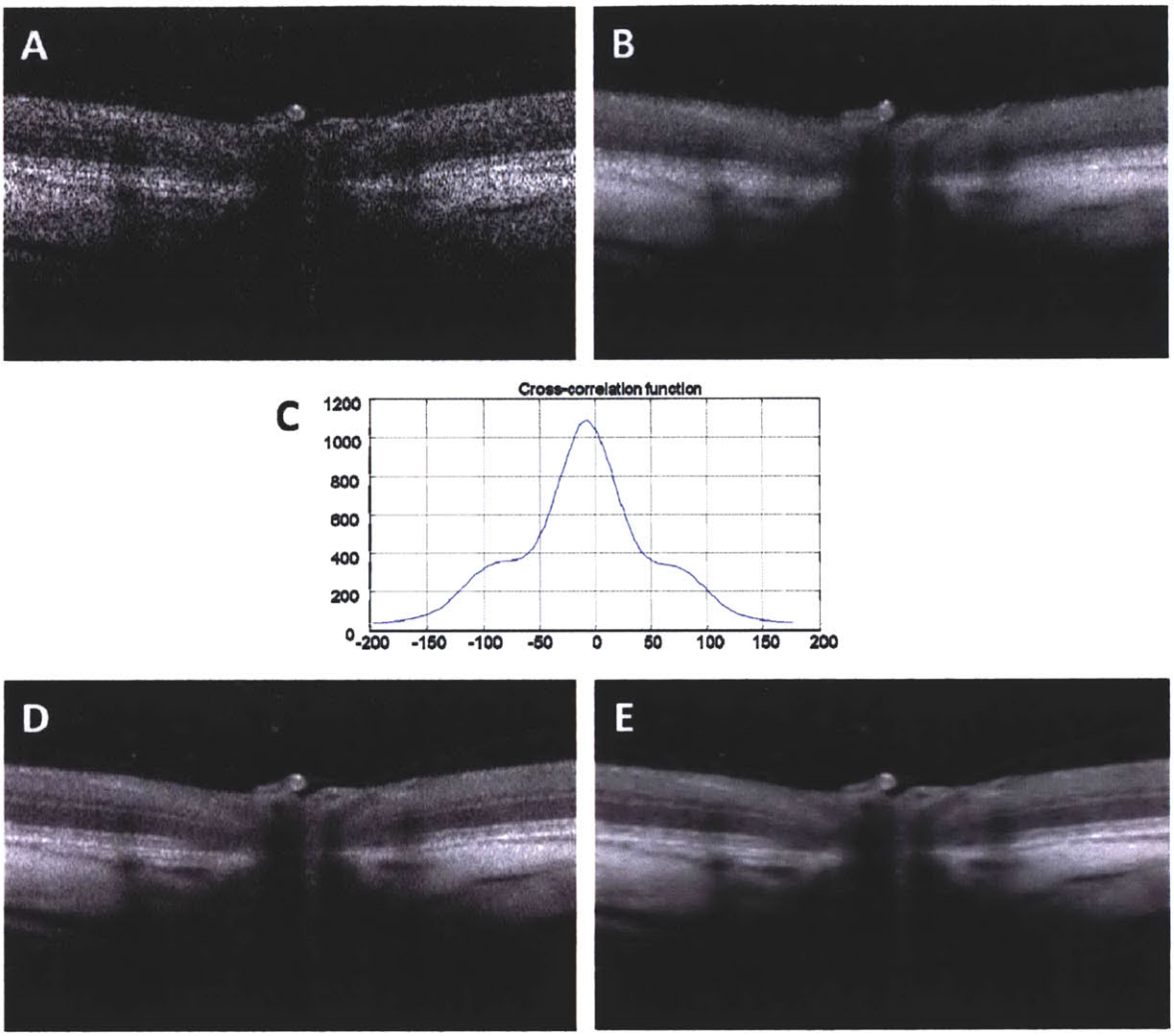

Figure 4-6. Speckle reduction by image averaging and median filtering. (A) An OCT cross-sectional image before speckle reduction. (B) An average of 10 neighboring cross-sectional images without image registration. (C) The cross-correlation function between the mean axial scans of two neighboring frames was calculated for rigid image registration. (D) An average of 10 neighboring cross-sectional images after rigid image registration for bulk motion removal. (E) A median filtered version of the image shown in (D). The size of the median filter was 3 pixels in the axial direction and 7 pixels in the transverse direction.

4.4 Results

Figures 4-2 and 4-3 show OCT images from 3D volumetric data sets acquired by the 650 nm and 750 nm channels of the dual-wavelength spectrometer, respectively. Note that the retina in the OCT images appears relatively flat in the lateral direction due to the OCT imaging interface with the pivot of scanning located at the pupil of the rat eye. The volumetric data sets consisted of 500 by 500 axial scans over an area of 1.2 mm by 1.2 mm centered at the optic nerve head. Because the two channels acquire images simultaneously, no registration between the data sets acquired at 650 nm and 750 nm in the transverse direction is required.

Figure 4-4 shows the roll-off characteristics of the 650 nm and 750 nm channels of the dual-wavelength spectrometer and the roll-off corrected OCT images from the two channels. The color map for the OCT images in Figure 4-4 is chosen to enhance visualization of the effect of roll-off correction on OCT cross-sectional images. The spectrometer roll-off was measured by imaging a single reflector at several different delay positions while ensuring that the reflected amount of light from the reflector remains constant. The continuous roll-off curves were generated by fitting the data points to a fifth order polynomial. Spectrometer roll-off correction was performed by dividing each of the axial scans in the OCT image with the continuous spectrometer roll-off curves.

Figure 4-5 shows the effect of wavelength-dependent absorption characteristics of Evans blue dye in the rat retina on OCT images. The *en face* projection images are created by summing intensity values of the volumetric data sets in the axial direction. Note that in general the color scale for the *en face* image from the 650 nm channel and that from the 750 nm channel are the same at a given time point. As can be seen, the brightness of the *en face* image from the 650 nm channel in relative to that from the 750 nm channel decreases over time. This is more clearly demonstrated by generating the ratio images which can be obtained by dividing the *en face* images acquired at 650 nm with those acquired at 750 nm.

Figure 4-6 demonstrates speckle reduction by image averaging and median filtering. Because of the involuntary eye motion during OCT imaging, bulk motion needs to be compensated by rigid

image registration before averaging multiple images. The images are averaged in the linear amplitude scale, but are displayed in the logarithmic scale due to the dynamic range.

4.5 Discussion

Measurement of Evans blue concentration *in vivo* using OCT requires simultaneous acquisition of data at two different wavelengths, preferably one at the absorption maximum and the other at the minimum. Therefore, a dual-wavelength spectroscopic OCT system shown in Figure 4-1 was developed to enable simultaneous acquisition of OCT images using the 650 nm and 750 nm channels of the spectrometer. As can be seen from the *en face* projection images in Figures 4-2 and 4-3, the two channels generate OCT images from the same scan area as desired, and no further registration between the data sets acquired at 650 nm and 750 nm is required. However, it should be noted that the OCT images from the 750 nm channel in general have slightly deeper tissue penetration depth into the choroid compared to the images from the 650 nm channel possibly due to the longer wavelength [7]. In addition, note that the axial positions of the anterior surface of the retina in the OCT images are slightly different for the two spectrometer channels because of optical dispersion from the water in the anterior part of the rat eye. Because this effect results in 750 nm OCT images farther away from the zero delay compared to 650 nm OCT images, the quality of the image acquired at 750 nm is affected even more severely by the spectrometer roll-off. However, because the system sensitivity is higher at 750 nm than at 650 nm, this effect was tolerable.

Spectrometer roll-off correction is an essential step for spectroscopic OCT data processing in order to decouple signal attenuation within tissue from signal attenuation due to spectrometer imperfection. However, there is one undesired effect of spectrometer roll-off correction. As can be seen from Figure 4-4, roll-off correction results in a rise in the noise level as a function of depth. Conceptually, OCT is supposed to have noise with zero mean everywhere in the image regardless of the presence of the signal. However, because the magnitude of the OCT signal is used in this study for generation of OCT images, noise where there is no signal does not have a zero mean because of the rectification resulting from taking the magnitude. It should be noted that this effect may affect quantitative measurement of Evans blue dye concentration using

spectroscopic OCT and should be accounted for when interpreting spectroscopic data. However, noise where there is signal whose magnitude is greater than that of noise still has zero mean while the variance of noise is always increased by roll-off correction in a depth-dependent manner. The variance of noise can be reduced by averaging multiple OCT images, which will be discussed later. The variance of noise can also be reduced by summing intensity values in the axial direction, as is done in generating OCT *en face* projection images, because noise from one pixel of an axial scan is not correlated to noise from another pixel.

After roll-off correction, spectroscopic OCT data sets can be assessed to detect the wavelength-dependency of Evans blue dye. As can be seen from Figure 4-5, intravascular injection of Evans blue dye results in increased shadowing from major blood vessels in the OCT images acquired from the 650 nm channel, while there is almost no change in the OCT images simultaneously acquired from the 750 nm channel. This can be clearly visualized from the normalized *en face* ratio images, which were obtained by dividing the OCT *en face* image acquired at 650 nm with the OCT *en face* image simultaneously acquired at 750 nm. For the baseline and immediately after CA-I injection, the normalized *en face* ratio images do not show any sign of increased shadowing from major blood vessels at 650 nm. This implies that the OCT signals in the blood vessel at 650 nm and 750 nm are attenuated by similar amounts in the absence of Evans blue dye. However, immediately after the injection of Evans blue dye, there is a significant decrease only in the OCT signal from the 650 nm channel, particularly at the major blood vessels. The effect becomes more pronounced even in the surrounding tissue where there is no major blood vessel 1 hour and 2 hours after the injection of Evans blue dye. Figure 4-5 confirms that wavelength-dependent signal attenuation due to Evans blue dye can be indeed detected by the dual-wavelength spectroscopic OCT system.

For quantitative mapping of vascular permeability, however, various sources of artifacts should be identified in the imaging system, and spectroscopic data processing methods should be developed further. Speckle and noise are examples of these artifacts. Figure 4-6 demonstrates that noise and speckle can be reduced significantly by averaging multiple neighboring OCT images. As discussed in Chapter 2, speckle in OCT is a phenomenon that is stationary in time provided that the sample is stationary. However, due to the involuntary eye motion caused by

heartbeat and breathing during OCT imaging, each OCT image has a slightly different speckle pattern from the other even if nominally the same area is scanned repeatedly. When this bulk eye motion is severe, it needs to be compensated by rigid image registration before averaging multiple images in order to maintain the axial resolution. Although the rigid image registration employed in this study does not correct for the bulk motion component in the lateral direction, bulk motion in the lateral direction is assumed to be negligible compared to that in the axial direction.

In order to obtain quantitative measurements of Evans blue leakage into the retinal space, it will be necessary to develop methods to analyze depth dependent absorption in cross-sectional OCT images. There are several factors which make this measurement challenging. Evans blue leakage occurs in both the vitreous and aqueous while the OCT beam path length in these structures is longer than in the retina. Therefore, it results in a parasitic source of absorption which must be removed from the measurement. Quantitative measurements of absorption in the retina may also be affected by Evans blue dye in the retinal vasculature including the capillary network, which must be separated from Evans blue absorption in retinal tissue. This will require developing methods which quantitatively normalize out absorption from different retinal layers.

In spite of these challenges, the preliminary results acquired to date are very promising. Since OCT provides depth-dependent intensity profile of the retina, combined with the Beer-Lambert absorption law, OCT is expected to provide a quantitative three dimensional vascular permeability map. The development of a spectroscopic OCT method for assessing changes in vascular permeability in small animal models would represent a significant advantage by reducing the amount of labor intensive analysis while enabling mapping of vascular permeability changes across the fundus and potentially even at the level of individual retinal layers.

References

1. Q. W. Xu, T. Qaum, and A. P. Adamis, "Sensitive blood-retinal barrier breakdown quantitation using Evans blue," Invest. Ophthalmol. Vis. Sci. **42**, 789-794 (2001).
2. D. Skondra, K. Noda, L. Almulki, F. Tayyari, S. Frimmel, T. Nakazawa, I. K. Kim, S. Zandi, K. L. Thomas, J. W. Miller, E. S. Gragoudas, and A. Hafezi-Moghadam,

"Characterization of azurocidin as a permeability factor in the retina: Involvement in VEGF-induced and early diabetic blood-retinal barrier breakdown," Invest. Ophthalmol. Vis. Sci. **49**, 726-731 (2008).

3. A. Saria and J. M. Lundberg, "Evans blue fluorescence - quantitative and morphological evaluation of vascular permeability in animal tissues," J. Neurosci. Methods **8**, 41-49 (1983).
4. T. Okamura, N. Ishibashi, T. S. Kumar, D. Zurakowski, Y. Iwata, H. G. W. Lidov, and R. A. Jonas, "Hypothermic Circulatory Arrest Increases Permeability of the Blood Brain Barrier in Watershed Areas," Ann. Thorac. Surg. **90**, 2001-2008 (2010).
5. E. D. F. Costa, E. B. Rodrigues, M. E. Farah, E. Dib, F. Penha, O. Magalhaes, B. A. Furlani, A. A. S. Lima, A. de Miranda, and M. Maia, "Vital Dyes and Light Sources for Chromovitrectomy: Comparative Assessment of Osmolarity, pH, and Spectrophotometry," Invest. Ophthalmol. Vis. Sci. **50**, 385-391 (2009).
6. B. B. Gao, A. Clermont, S. Rook, S. J. Fonda, V. J. Srinivasan, M. Wojtkowski, J. G. Fujimoto, R. L. Avery, P. G. Arrigg, S. E. Bursell, L. P. Aiello, and E. P. Feener, "Extracellular carbonic anhydrase mediates hemorrhagic retinal and cerebral vascular permeability through prekallikrein activation," Nature Medicine **13**, 181-188 (2007).
7. B. Povazay, K. Bizheva, B. Hermann, A. Unterhuber, H. Sattmann, A. F. Fercher, W. Drexler, C. Schubert, P. K. Ahnelt, M. Mei, R. Holzwarth, W. J. Wadsworth, J. C. Knight, and P. S. Russel, "Enhanced visualization of choroidal vessels using ultrahigh resolution ophthalmic OCT at 1050 nm," Optics Express **11**, 1980-1986 (2003).